中央大学博士論文

Development of Lunar or Planetary Subsurface Exploration Robot Using Peristaltic Crawling

Hayato Omori
大森　隼人

博士（工学）

中央大学大学院
理工学研究科
精密工学専攻

平成２５年度
２０１４年3月

Development of Lunar or Planetary Subsurface Exploration Robot Using Peristaltic Crawling

Hayato Omori

Doctor of Engineering

Doctoral Program in Precision Engineering Course

Graduate School of Science and Engineering

Chuo University

March 2014

Contents

Chapter 1: Introduction **1**
1.1 Background 1
1.2 Motivation 4
1.3 Research Contributions 5
1.4 Outline of Dissertation 6

Chapter 2: Related Research **9**
2.1 Excavation Machinery on the Earth 9
2.2 Subsurface Exploring on the Moon 10
2.3 Previous Research about Subsurface Explorer 13
2.3.1 Classifications of Explorers 13
2.3.2 Effect of the Earth Pressure for Propulsion 19
2.3.3 Novel Concept for excavator 22

Chapter 3: Peristaltic Crawling of an Earthworm **23**
3.1 Mechanism of the Peristaltic Crawling 23
3.2 Measurement of an Actual Earthworm's Peristaltic Crawling 24

Chapter 4: Concept of a Novel Subsurface Explorer Robot **26**
4.1 Mechanism of a Novel Subsurface Explorer Robot 26
4.2 Excavation Motion in Future Missions 27

Chapter 5: Development of an Excavation Unit **30**
5.1 Development of Tapering Earth Auger 30
5.2 Tracks of Tapering EA 31
5.3 Volume of Soil Inside EA 34
5.3.1 Volume Modeling of Soil Inside EA 34
5.3.2 Results of Calculation 40
5.4 Development of Excavation Unit 41
5.5 Excavation Experiment Setup 41
5.6 Excavation Experiments 45
5.6.1 Changing the Pushing Force 45
5.6.2 Changing Rotation Speeds 47
5.6.3 Comparisons of the Effect of Earth Pressure and Experimental Results 48
5.6.4 Conclusion of Experiments with Excavation Unit 49

Chapter 6: Development of a Propulsion Unit 50
6.1 Development of a Propulsion Subunit 50
6.2 Experiments with Actuated Ring 54

Chapter 7: Development of Subsurface Explorer 57
7.1 Prototype Robot Integrating Propulsion and Excavation units 57
7.2 Control System 59
7.3 Propulsion Velocity 59
7.4 Propulsion Experiments in a Pipe 60
7.5 Excavation Experiments 61
7.5.1 Experimental Setup 61
7.5.2 Experimental Results for Various Excavation Conditions 62
7.6 Excavation Experiments with Dirt Collector 65

Chapter 8: Development of a Discharging Part 67
8.1 Development of a Prototype Discharging Part 67
8.2 Discharging Experiments 69
8.3 Discharging Experiment with an Excavation Robot 70
8.4 Discussion of the Results 72

Chapter 9: Fundamental Experiments for Modelling the Cutting Resistance 73
9.1 Definition of Excavation Resistance 73
9.2 Experimental Conditions 74
9.3 Experimental System 76
9.4 Pushing and Rotation Experiments with EA 77
9.4.1 Conditions for Pushing and Rotation Experiments 78
9.4.2 Pushing Force Experiments 78
9.4.3 Rotation Speed Experiments 80
9.4.4 Discussion of Soil Cutting Experiments 81
9.5 Depth Experiments with Screw Part 82
9.6 Soil Cutting Experiments with the Fish Tail 84
9.6.1 Measurement of Pushing Force Distribution 84
9.6.2 Measurement of Torque of the Fish Tail 85
9.7 Evaluation of Excavation with Mechanical Specific Energy 87

Chapter 10: Conclusion 89
10.1 Summary of Dissertation 89
10.2 Future Work 91

Appendix A: Characteristic of the Moon 93
A1 Physical Properties of the Moon 93

A2 Lunar Regolith 94
A2.1 Lunar Regolith 94
A2.2 Sampled Regolith 94
A3 Bulk Density and Relative Density 95
Appendix B: Hardware References (Paper version only) 97
B1 Maxon EC-max 30 97
B2 Wire Sensor (WDS-1000-C3-P, Micro-Epsilon) 98
B3 AD Board (PCI 3153, Interface) 99
B4 Stepping Motor (MB0401, KSS) 100
B5 Motor Driver (KR-A5CC, KSS) 101
B6 H8 / 3052F 102

References I
Publications VIII
Acknowledgements XIII

Chapter 1: Introduction

1.1 Background

Years and years ago, our ancestors looked up at the sky and saw millions of stars. They grouped the stars into figures, animals or objects, gradually seeing them as constellations. More recently, we have discovered significant important facts and objects such as geocentrism and planets. In addition, our spirit of exploration could not be suppressed. The Soviet Union launched the first satellite, Sputnik 1 (Fig. 1.1), in 1957 in orbit around the Earth [2]. Two years later, in 1959, they launched the probe Luna 2 (Fig. 1.2), which crashed into the Moon. Finally, astronaut Yuri Gagarin, on board Vostok 1 became the first human to travel into space in 1961 [4]. After that, Luna 9 became the first spacecraft to achieve a landing on the Moon in 1966. Table 1.1 shows a list of moon landers, which investigated lunar soil properties or collected samples using equipment such as a scoop or a core tube [5]–[10]. Surveyor was equipped with the soil surface sampler that consisted of a scoop [11], [12]. The scoop was set to get rid of lunar surface soil to a depth of 20 cm in order to observe the underlying material and conditions with a television camera. About one year after Surveyor 7, the first humans were sent onto the lunar surface with Apollo 11 in 1969. Apollo missions continued

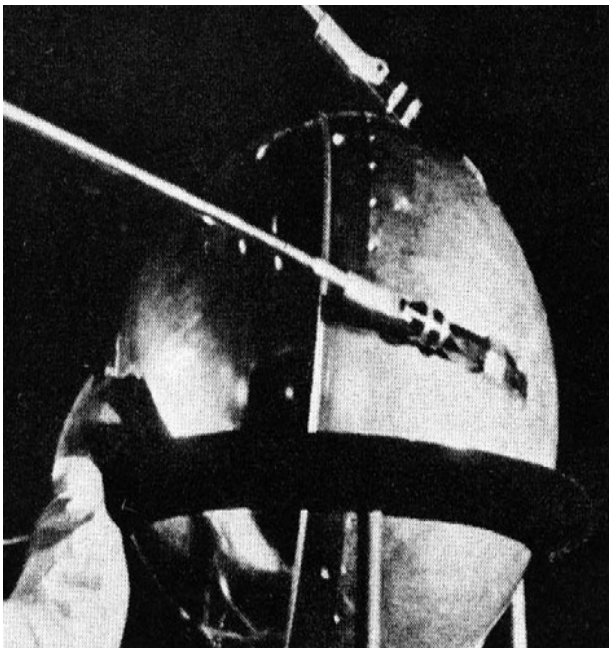

Fig. 1.1 Sputnik 1 [1]

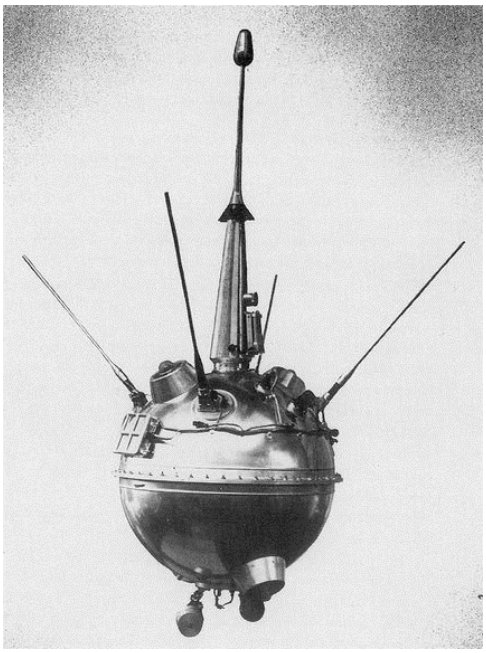

Fig. 1.2 Luna 2 [3]

sending astronauts to the Moon till the end of 1972. They took underground regolith samples to a depth of around 3 m using a core tube [13]. Manned missions enabled the return of large samples of regolith and rocks to the Earth. At the same time, The Soviet Union conducted unmanned space missions which they called the Luna programme. The Luna 16 mission was the first attempt to return a regolith sample from a depth of 35 cm. The Soviet Union also succeeded in using a rover which could conduct *in-situ* soil mechanics investigations. In the end, they were able to drill to a depth of 160 cm and bring back samples (Fig. 1.7 [14] and Fig. 1.8 [15]). The Apollo and Luna samples made it possible to know the age and composition of the Moon, and to propose new hypotheses about the Moon's origin.

Fig. 1.3 Vostok 1 [4]

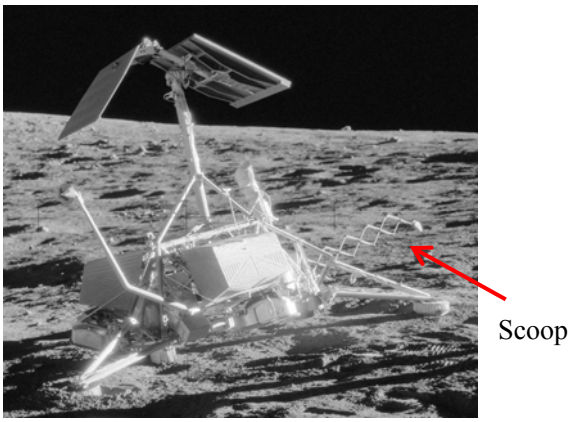

Fig. 1.4 Surveyor 3 on the Moon [11]

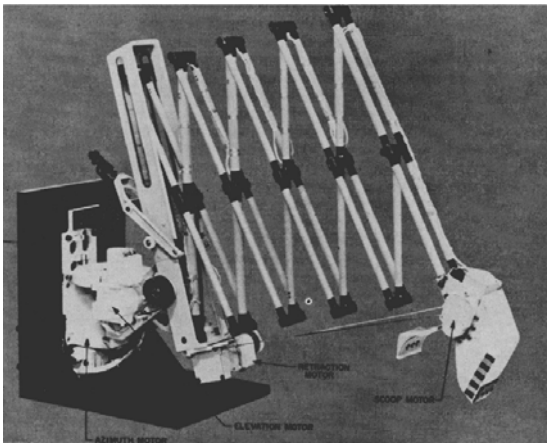

Fig. 1.5 Surveyor soil mechanics surface sampler [12]

Table 1.1 List of lunar regolith investigations [5]–[10]

S: Sample returned to the Earth, SM: Soil mechanics studies

Mission	Launch date	Landing data	Type	Reached Depth [cm]	Mechanism	Data	Returned sample [kg]
Surveyor 3	1967.04.17	1967.05.20	Unmanned lander	17.5	Scoop	SM	-
Surveyor 5	1967.09.08	1967.09.11	Unmanned lander	1-20	Scoop	SM	-
Surveyor 6	1967.11.07	1967.11.17	Unmanned lander	1-20	Scoop	SM	-
Surveyor 7	1968.01.07	1968.01.10	Unmanned lander	1-20	Scoop	SM	-
Apollo 11	1969.07.16	1969.07.24	Manned lander	13.5	Core tube	S, SM	21.6
Apollo 12	1969.11.14	1969.11.24	Manned lander	31.6	Core tube	S, SM	34.3
Luna 16	1970.09.12	1970.09.17	Unmanned lander	35	Drill tube	S	0.1
Luna 17	1970.11.10	1970.11.17	unmanned lander and rover	5	Penetrator	SM	-
Apollo 14	1971.01.31	1971.02.09	Manned lander	70	Core tube	S, SM	42.3
Apollo 15	1971.07.26	1971.08.07	Manned lander and vehicle	237	Core tube	S, SM	77.3
Luna 20	1972.02.14	1972.02.21	Unmanned lander	25	Drill	S	0.05
Apollo 16	1972.04.16	1972.04.27	Manned lander and vehicle	221	Core tube	S, SM	95.7
Apollo 17	1972.12.07	1972.12.11	Manned lander and vehicle	292	Core tube	S, SM	110.5
Luna 21	1973.01.08	1973.01.15	Unmanned lander and rover	-	Penetrator	SM	-
Luna 24	1976.08.09	1976.08.18	Unmanned lander	160	Drill tube	S	0.17

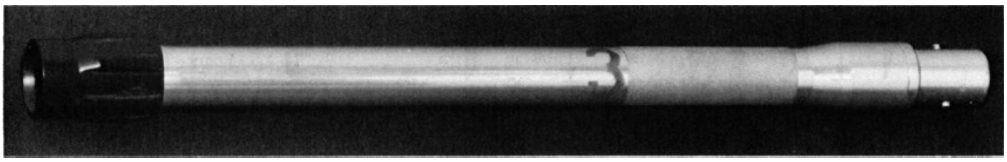

Fig. 1.6 Core tube sampler during Apollo 11 mission [13]

Fig. 1.7 Lander during Luna 24 [14]

Fig. 1.8 Drilling system during Luna 24 [15]

Recent years, most of aerospace explorer's missions have been carried out with unmanned space probes such as a spacecraft or a rover. For example, the Mars rover Curiosity, unmanned, was equipped with several in-situ analytic instruments [16]. It successfully bored a 64 mm hole in the Martian bedrock and obtained samples in 2013 [17]. The Hayabusa, an unmanned spacecraft developed by JAXA, landed on an asteroid called "Itokawa" in 2005 [18]. It successfully collected samples and took them back to the Earth in 2010 [19]. The samples were analysed in detail and demonstrated that Itokawa [20] and majority of meteorites that fall to the Earth came from S-class asteroids [21].

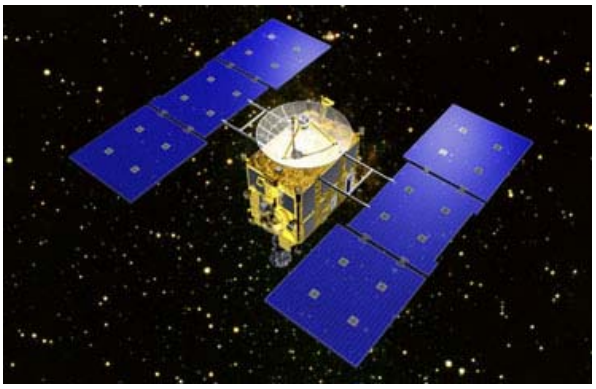

Fig. 1.9 Image of Hayabusa [18]

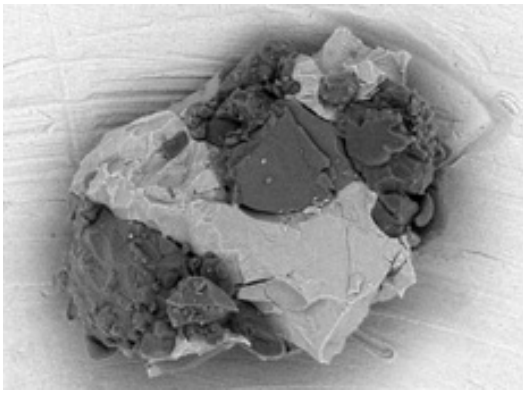

Fig. 1.10 Sample of Itokawa [19]

1.2 Motivation

In 2013, space agencies participating in the international space exploration coordination ground (ISECG) developed a global exploration roadmap (Fig. 1.11), which indicates international collaborative space exploration missions [22]. As seen in the figure, the goal of exploration is Mars, missions of the International Space Station (ISS), the Moon and Asteroids Activities for accomplishment are divided into five areas: ISS utilization, robotic missions, advanced technologies, next generation capabilities and analogues. It can be seen that the Moon exploration mission plays an important role and is placed in the early and middle stages.

As demonstrated on the Apollo and the Luna projects, the Curiosity, the Hayabusa, aerospace explorations have great potential. It can lead to new discoveries, such as new substances, or help to find keys to the origin of our planet. Planetary and asteroid investigations have provided basic information about the planets, such as geological, magnetic, and gravitational properties. However, many territories remain unexplored, particularly underground. Thus, scientific progress should be made in this area. However, some types of explorers launched from Planet Earth may take a long

time to reach another planet. Small unmanned explorers will therefore be needed first, both for safety and economic reasons. The Moon is the best-explored astronomical object whose importance has been demonstrated by ISECG. Many explorers and robots have been placed on its surface as introduced before. All this remains very limited though. The aim of this dissertation is therefore development of a small underground explorer that would be suitable for carrying out such important tasks on a larger scale.

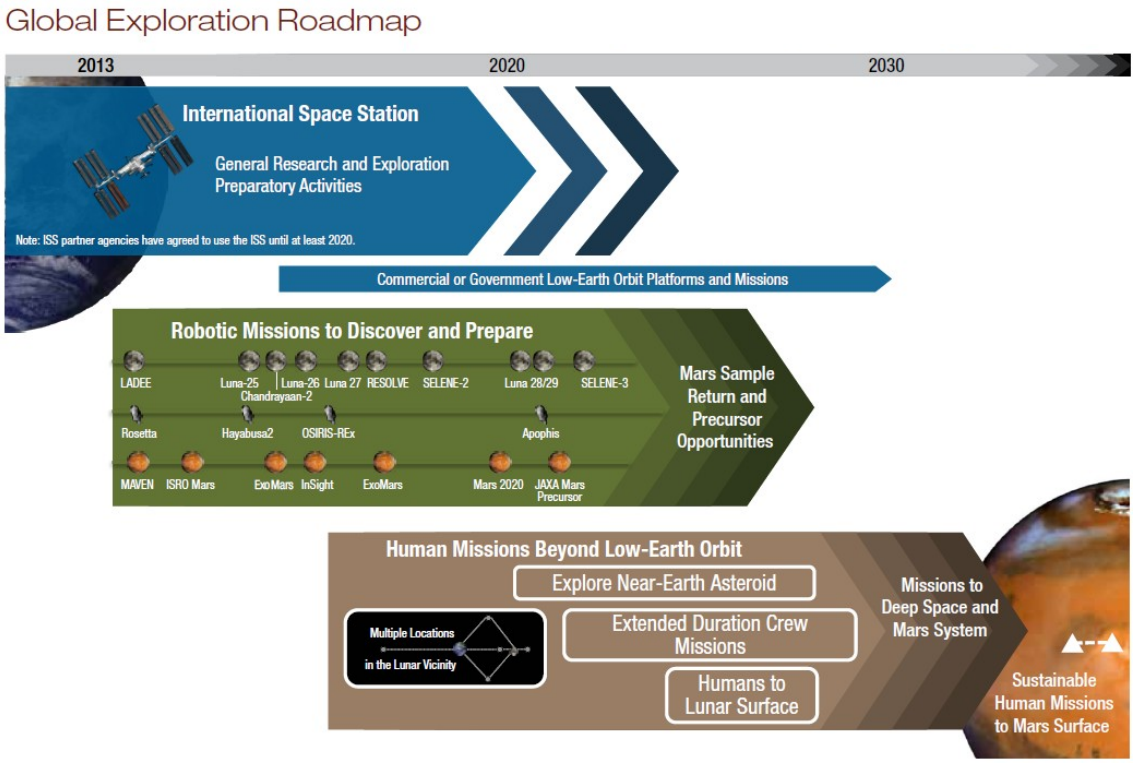

Fig. 1.11 Global space exploration roadmap by ISECG [22]

1.3 Research Contributions

The main goal of this dissertation is the development of an excavation robot for lunar and planetary subsurface explorer missions. It could conduct sampling material and setting scientific devices underground, has a feature of small in size and light weight. The contributions of this dissertation are listed as follows:

Robot with a propulsion unit based on the peristaltic crawling of an earthworm

This robot has a propulsion unit with the peristaltic crawling of an earthworm. In order to excavate underground, this unit composes of novel mechanisms: dual pantograph mechanism and large space

inside for excavation unit.

Robot with an excavation unit based on an earth auger

The excavation unit is based on an earth auger (EA). New type of EA has a tapering shape in the front to combine with the propulsion unit. This unit enables smooth excavation with making space for propulsion and discharging from the rear of the robot.

Robot with propulsion and excavation units

The robot with propulsion and excavation units can control excavation velocity and excavation torque due to the propulsion unit. In addition, the robot is able to excavate with lighter weight such as 1/6 of its own weight by experiments, which shows a great possibility to conduct future missions on the Moon that has 1/6 of lighter gravity than on the Earth.

Excavation process of the front part of the earth auger

Excavation experiments of the front part of the earth auger are conducted to reveal the process of excavation in several conditions. Efficiency of excavation is evaluated using the mechanical specific energy.

1.4 Outline of Dissertation

This section introduces the outline of dissertation following each chapter. Fig. 1.12 shows the flow chart of the outline.

Chapter 2: Related Research

This chapter introduces and discusses related excavation technologies such as some heavy machinery used on the Earth and excavators for the Moon and planets. Then mechanism and performance of various small excavators are compared and discussed.

Chapter 3: Peristaltic Crawling of an Earthworm

This chapter describes the peristaltic crawling of an earthworm because a developed excavation robot uses its motion as a propulsion unit. Therefore, the locomotion of an actual earthworm is analysed.

Chapter 4: Concept of a Novel Subsurface Explorer Robot

This chapter describes a detailed concept of a novel subsurface explorer robot which has propulsion and excavation units based on the peristaltic crawling of an earthworm and earth auger, respectively. Detail mission process is demonstrated with full use of mechanism. The advantages of the robot are formulated.

Chapter 5: Development of an Excavation Unit

This chapter first presents the development of tapering earth auger including mathematical model of EA and volume inside soil. Next, an excavation unit is developed and conducted experiments:

pushing force and rotation speeds. From the results, the reached depth and motor torque represented excavation resistance are measured. The depth prediction in terms of the earth pressure around the unit is introduced. These values are used to discuss the results.

Chapter 6: Development of a Propulsion Unit

This chapter first introduces the developed earthworm robots. Next, a single unit of the propulsion unit with a pantograph mechanism and large space in the middle for an excavation unit is developed and tested to measure performance in several conditions and environments.

Chapter 7: Development of a Subsurface Explorer

In this chapter, the subsurface explorer with connected a propulsion and excavation units is developed. The propulsion velocity is modelled and evaluated with experiment in a pipe. Next it conducts excavation experiments with 1/6 of its own weight using a counter weight from a launcher as explained for the future mission (Chapter 4) until the discharge ports reaches the surface level. It also showed a great excavation performance. Finally, excavation experiment is reported after a depth of the discharge ports reached the surface level, now getting rid of the excavated soil using a dust collector.

Chapter 8: Development of a Discharging Part

To address the issue of discharging for deep excavation (deeper than when the discharge ports reach the surface level), a discharging part is developed. First, experiments are conducted inside a launcher and the number of winching and soil dropped rate are also measured to evaluate the performance. Finally, excavation experiments with the propulsion and excavation unit is conducted.

Chapter 9: Fundamental Experiments for Modelling the Cutting Resistance

For modelling the cutting resistance, cutting experiment with the earth auger is conducted in this chapter. First, purpose and definition of cutting resistance are explained. In experiments, the effect is classified: pushing force and cutting depth on the screw part, and that on the fish tail. A 6 axis sensor measures the torque and vertical force. In the end, the excavation performance is evaluated using mechanical specific energy.

Chapter 10: Conclusion

This chapter summarises the paper by chapter. Future work is mentioned about the cutting model, mechanism for mounting a sampler and scientific devices, and strategies of horizontal direction excavation.

Chapter 1: Introduction

Chapter 2: Related Research

Chapter 3: Peristaltic Crawling of an Earthworm

Chapter 4: Concept of a Novel Subsurface Explorer Robot

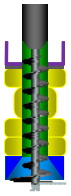

Chapter 5: Development of an Excavation Unit

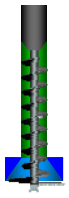

Chapter 6: Development of a Propulsion Unit

Chapter 7: Development of a Subsurface Explorer

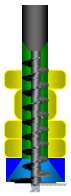

Chapter 8: Development of a Discharging Part

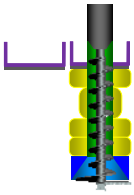

Chapter 9: Fundamental Experiments for Modelling the Cutting Resistance

Chapter 10: Conclusion

Fig. 1.12 Flow chart of the outline

Chapter 2: Related Research

2.1 Excavation Machinery on the Earth

We usually use an excavator with bucket (Fig. 2.1), boring machine (Fig. 2.2) and shield machine (Fig. 2.3) on the Earth in construction field. The excavator with bucket can excavate deep depth at one time but it requires a complex system for an automatic control and a large size of the machine. A boring machine is used to investigate basement formations. Because the length of the drilling tools must be sufficient to reach the desired depths, the size of the machine must be large. A shield machine is used to make a tunnel. It covers the excavated hole with a wall to prevent from a hole collapsing, which requires to carry lots of material for the wall. Therefore, these types of machinery are not useful for aerospace missions.

Fig. 2.1 Excavator with bucket [23]

Fig. 2.2 Boring machine [24]

Fig. 2.3 Shield machine [25]

2.2 Subsurface Exploring on the Moon

Many different types of robots and machines have been developed in order to investigate underground of planets. These different subsurface exploring methods are classified into three and are shown in Fig. 2.4. (a) Surface base excavator, such as the Mars Surface Sample Transfer and Manipulation (MSSTM) [26] and LSAS [27], which have a main platform on the surface of a planet. This platform has an actuator to control the excavation. Their excavation system is difficult to excavate deep with a large diameter of hole because the drill and the platform is connected. The same length of drill as the desired depth is need. In case of drilling deep, the drill diameter should be small to make the whole system small. (b) Penetrator: JAXA planned to use two penetrators in its Lunar-A project (Fig. 2.7) [28]. The similar penetrator is proposed in MoonLITE project (Fig. 2.8) [29]. The penetrators, which contained seismometers and heat-flow probes, would be loaded on a spacecraft. However, the proposed system did not have any mechanism to adjust the attitude and depth of the penetrators after impact, and they would largely disturb the original conditions of the surroundings at the impact time. A micro-penetrator (Fig. 2.9) [30], which is a type of explorer, consists of a drill and sampler subsystem. This system is expected to drill a small hole having diameter 1–2 m, deep into the surface, using low power and would be equipped with several scientific devices. However, as it drills deeper, the buckling problem in the drill becomes severe. Other crucial issues of penetrators are no propulsion once it stops and no reusable. (c) Subsurface explorer: an excavation robot controls the excavation and propulsion while the robot itself is burrowing. The small size robot would carry out the excavation mission with a sample collecting and scientific devices. Therefore, this type would meet the request for planetary subsurface explorer. Moreover, it would be used not only for a planetary subsurface explorer but for an excavator on the

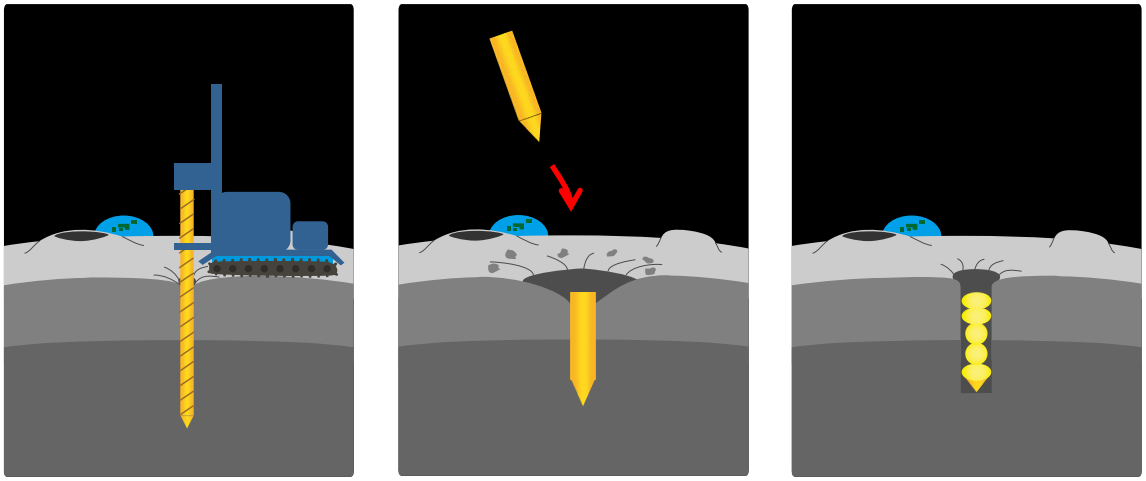

a) Surface base excavator b) Penetrator c) Subsurface explorer

Fig. 2.4 Subsurface exploring methods

Earth e.g., on the ground and in the water. Varieties of designed and developed subsurface explorers are introduced in the next section.

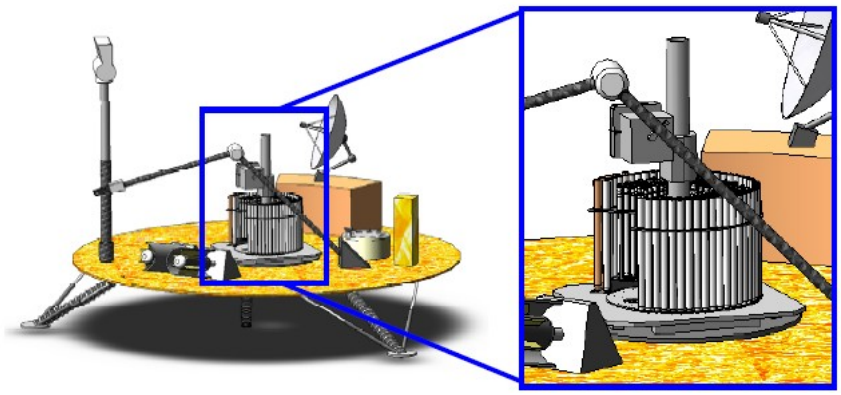

Fig. 2.5 Shield machine Mars Surface Sample Transfer and Manipulation (MSSTM) [26]

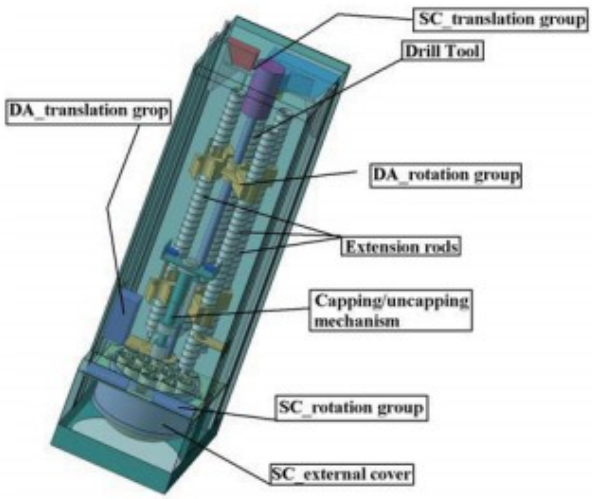

Fig. 2.6 LSAS [27]

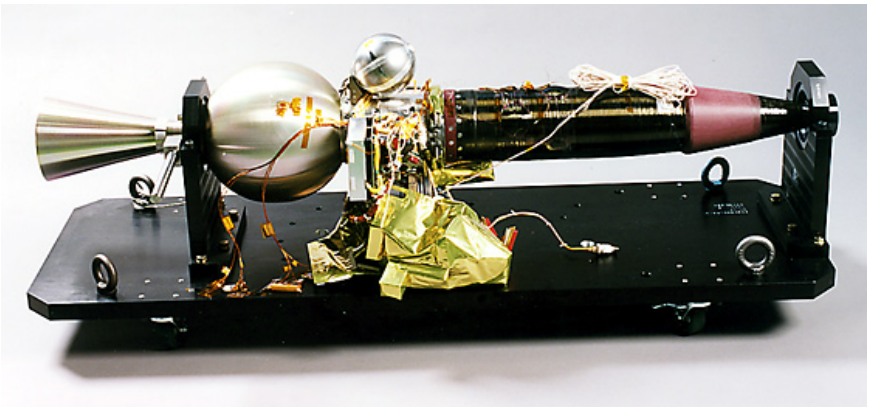

Fig. 2.7 Penetrator in Luna-A [28]

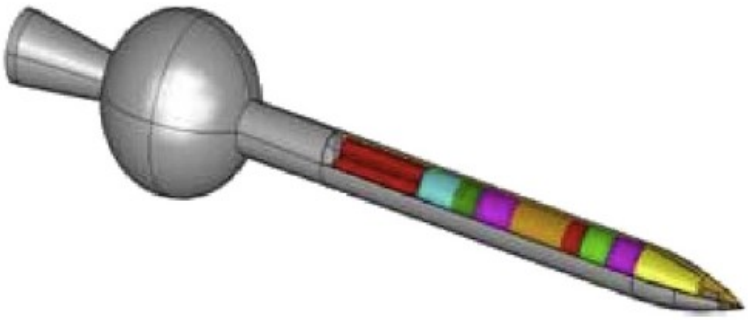

Fig. 2.8 Penetrator in Moon-LITE project [29]

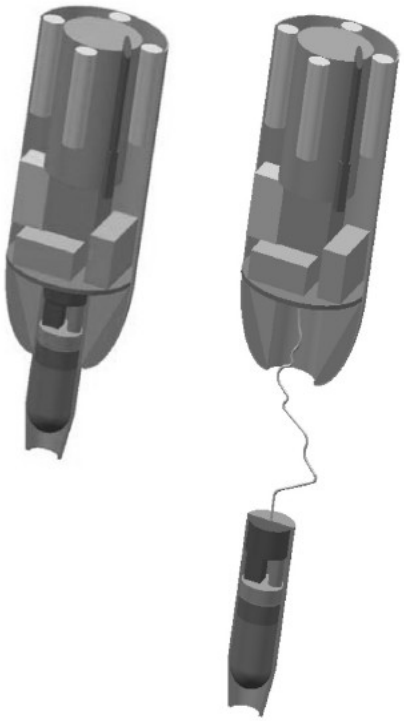

Fig. 2.9 Micro-penetrator [30]

2.3 Previous Research about Subsurface Explorer

2.3.1 Classification of Explorers

This section demonstrate small subsurface explorer robot which have been designed and developed by other researchers. Fig. 2.10 – 2.22 shows each robots and Table 2.1 shows the references, specifications, mechanisms and excavation targets. Fig. 2.23 shows mechanical comparisons of the robot followed by excavation process [31]. Their two classifications are first: a robot needs to make a space for moving downward, second: it needs to move forward to the space in front.

Fig. 2.24 shows the depth reached by various robots that have been developed, as well as those that have just been designed [32]. The part above the blue line shows robots that have been designed but have not yet been developed, whereas the part below the line shows the depths reached in excavation experiments by developed robots. The designed robots are plotted along the abscissa by the average diameter and the developed robots are plotted by average diameter against depth reached.

One of the smallest excavators is the planetary underground tool (PLUTO) [33] – [36], which uses a spring-loaded hammer having a diameter of 20 mm, a length of 280 mm, and a mass of 0.35 kg. These features enable it to successfully excavate to a depth of around 2000 mm in simulated Martian soil. However, it does not have much space for scientific devices, except for a sampling device at the top. The earthwormlike exploratory robots [37] – [38] have been designed with the peristaltic crawling of an earthworm for a propulsion mechanism but any specifications and excavation target have not explained. MOGURA2001 [39] – [42] consists of an excavating unit (blade) in front and a soil removal unit inside the robot. The excavation ability depends on the pushing force, which corresponds to its weight, because it does not have a supporting unit for propulsion. It could reach a depth of around 300 mm. The Moon Mars underground mole (MMUM) [43] – [44] was based on a spring-loaded hammer similar to the one used in PLUTO. It is about twice as large in size as PLUTO and has a mass of 2 kg. MMUM could reach a depth of around 500 mm in gritty dry sand. Two mole-type robots have also been developed. The other mole robot was proposed by Kubota et al. [45] – [47]. This robot excavates front soil with a drill and transport using screw with vibration. The discharged soil at the end of the robot is used to generate propulsion force with pushing the soil. They discussed a method for excavating, and demonstrated a robot's ability to carry and discharge soil using a test model, although no excavation data from their robot were reported. The inchworm deep drilling system (IDDS) [48] – [49] that has drill and inchworm propulsion mechanism was designed to drill deep into soil, ice, and rocks, mainly for exploring Mars and Europa. It is expected to excavate to a depth of 0.001–1 km because of its lack of tether or umbilical cord, although no data of any actual excavation depths have been presented. A detailed design for the robotic planetary drilling system-smart space drilling system (RPDS / SSDS) [50] included a propulsion unit, drill bit, and cuttings bucket. This robot collects the excavated material in the bucket and returns to the

surface using wheels for discharging. It was designed according to typical, recommended specifications in terms of energy requirements [51] and was capable of moving along a curved path. However, this system has not yet been demonstrated. A screw subsurface explorer [52] – [54], which has simple mechanism, is completely covered with screws. Front and rear screws rotate in opposite directions, which prevents the robot from rotating. The screw propulsion force is also used as a propulsion force for the robot. It could excavate 120 mm into fly ash, but stopped because of a structural issue. Yasuda et al. have developed a second prototype of the self-turning screw mechanism (STSM) [55] – [58], which has a diameter of 120 mm. A wheel inside the body rotates and this fast rotation is stopped using a clutch. The robot rotates by a reactive torque because the clutch is connected to the body. A spiral blade around the body can generate a propulsion force in the soil. It was able to drill to a depth of 812.6 mm in fly ash in the case of the robots that are 1/6th of their own weight is used as counterweights to simulate the smaller gravity on the Moon relative to the Earth. However, it consumes the power of 100 W. The DIGBOT [59], which uses contra-rotating drill similar mechanism as the screw subsurface explorer, has a diameter of 50 mm. The robot has two drills that rotates in opposite directions not to rotate the body generates propulsion force and making a space at the same time. It could excavate 380 mm but the material information and condition has not been explained. The lunar wormbot [60] has a similar design to the wormlike exploratory robots and composed of the propulsion mechanism of the peristaltic crawling of an earthworm and the excavation mechanism of the drilling head. The drilled soil in front pushed the surrounding of the robot to make a space. Excavation experiments of the drill part have been carried out using flour but tests of the whole robot has not yet to be conducted. The crab robot agile burrowing olfactory testbed (CRABOT) [61] is based on excavation mechanism of a mole crab. To realize this mechanism, it has two paddle-like vanes composed of a flexible vane and a comb. The flexible vane is sustained by a comb and pushes the soil when the vane moves in one direction. By contrast, the flexible vane is not sustained, bends and allows the soil to pass through the comb when it moves in the opposite directions. However, the experiments were conducted on the surface of sand. Excavation experiments in vertical downward direction have not yet conducted. The auto-gopher [62] has been developed to excavated hard materials such as for the Mars, Europa and Enceladus not for soil. It excavates the material with a drill which is sustained by inchworm-like mechanism and collects it inside the robot. The robot is rewinded to the surface for discharge the collected material.

By considering these previous robot designs, it can be inferred that as the excavator becomes larger, it is more difficult to excavate deep into the soil. It is believed the friction around it increases and prevents it from tunneling deep [42]. Therefore, excavation depth is modeled in terms of size of an excavator and weight using lateral earth pressures of Coulomb.

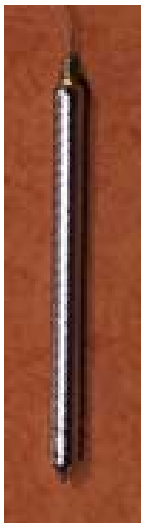

Fig. 2.10 Pluto [34]

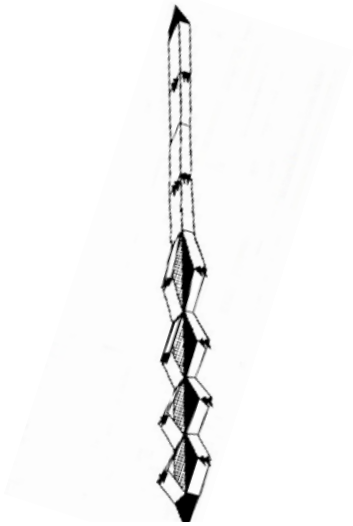

Fig. 2.11 Earthwormlike Exploratory Robots [38]

Fig. 2.12 MOGRA 2001 [41]

Fig. 2.13 MMUM [44]

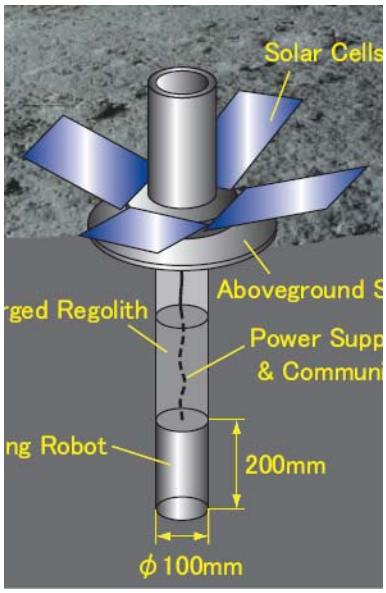

Fig. 2.14 Mole type [45]

Fig. 2.15 IDDS [48]

Fig. 2.16 RPDS / SSDS [50]

Fig. 2.17 Screw Subsurface Explorer [52]

Fig. 2.18 STSM [58]

Fig. 2.19 DIGBOT [60]

Fig. 2.20 Lunar Wormbot [61]

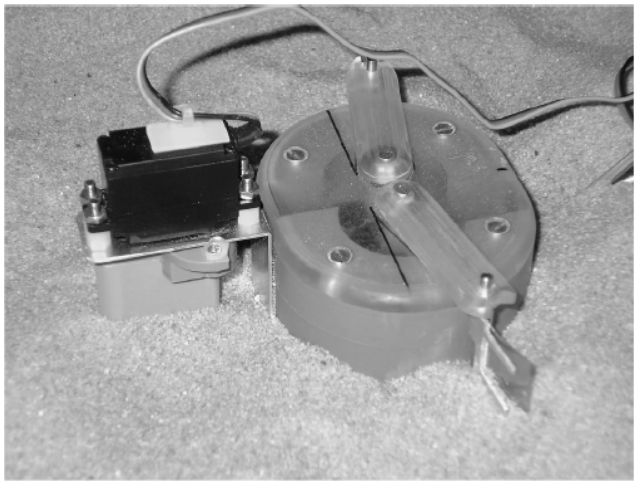

Fig. 2.21 CRABOT [62]

Fig. 2.22 Auto-Gopher (Courtesy Kris Zacny, Honeybee Robotics)

Table 2.1 Detail specifications of subsurface excavation robots

No.	Robots	Years and references	Excavation and propulsion strategies			Dia. Max. /Min.	Length	Mass	Power	Reached depth	Targets (materials)	Tested materials
			Make a space	Transport	Advance forward	mm	mm	kg	W	mm		
①	PLUTO	1997[33], 2001[34], 2002[35], 2004[36]	Soil compression / Pushing aside	None	Hammering mechanism	20 / 20	280	0.35	3	2000	Martian regolith	Flintage-Quartz sand mixture
②	Earthwormlike Exploratory Robots	1998[37], 1999[38]	Soil compression / Pushing aside	-	Earthworm	-	-	-	-	-	-	-
③	MOGRA 2001	1999[39], 2000[40], 2001[41], 2002[42]	Blades	Bucket	Own mass	270 / 160	300	8.3	up to 40	300	Moon (Regolith)	Simulant
④	MMUM	2003[43], 2007[44]	Soil compression / Pushing aside	-	Hammering mechanism	40	600	2	10	-	Moon / Mars	silica dry-sand
⑤	Mole type	2003[45], 2005[46], 2007[47]	Drill	Vibration	Pushing rear discharged soil	100	270	-	-	-	Moon (Regolith)	-
⑥	IDDS	2003[48], 2004[49]	Drill	Screw	Inchworm	150 / 100	1000	-	500-1000	-	Mars	-
⑦	RPDS / SSDS	2006[50]	Drill	Bucket and carriage	Wheels	160 / 150	500	50	570	-	Mars / Moon	-
⑧	Screw Subsurface Explorer	2006[51], 2009[52], 2010[53],	Screw drill	Screw	Screw propulsion	124 / 95	290	3.87	-	120	Moon (Regolith)	Fly ash
⑨	STSM	2008[54], 2010[55], 2011[56], 2012[57], 2013[58]	Screw drill	Screw	Screw propulsion	120	632	11	100	812.6	Moon (Regolith)	Fly ash
⑩	DIGBOT	2010[59]	Screw drill	Screw	Screw propulsion	50 / 30	200 - 300	-	-	380	Moon	-
⑪	Lunar Wormbot	2011[60]	Screw drill	-	Earthworm	160 / 113.1	-	-	-	-	Moon (Regolith)	Flour (Drilling test)
⑫	CRABOT	2011[61]	Pushing aside	Paddle	Paddle	70	55	-	-	-	Earth	Sand(0.06-2 mm)
⑬	Auto-Gopher	2013[62]	Drill	Carriage	Inchworm	71	1810	22	up to 100	2000	Mars / Europa / Enceladus	Rock

Fig. 2.23 Mechanism comparisons of the robots [64]

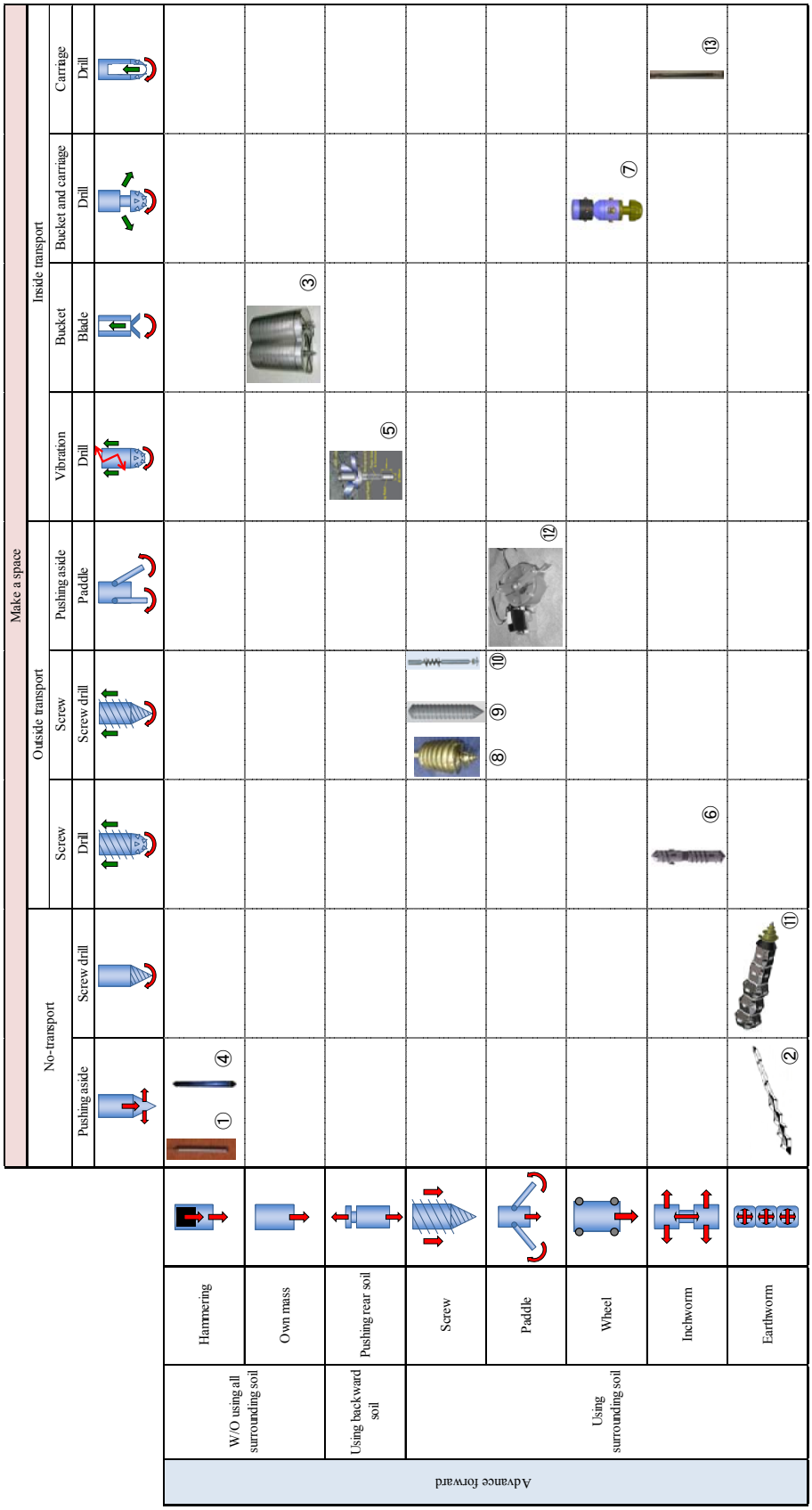

① PLUTO, ② Earthwormlike Exploratory Robots, ③ MOGRA 2001, ④ MMUM, ⑤ Mole type, ⑥ IDDS, ⑦ RPDS / SSDS, ⑧ Screw Subsurface Explorer, ⑨ STSM, ⑩ DIGBOT, ⑪ Lunar Wormbot, ⑫ CRABOT, ⑬ Auto-Gopher

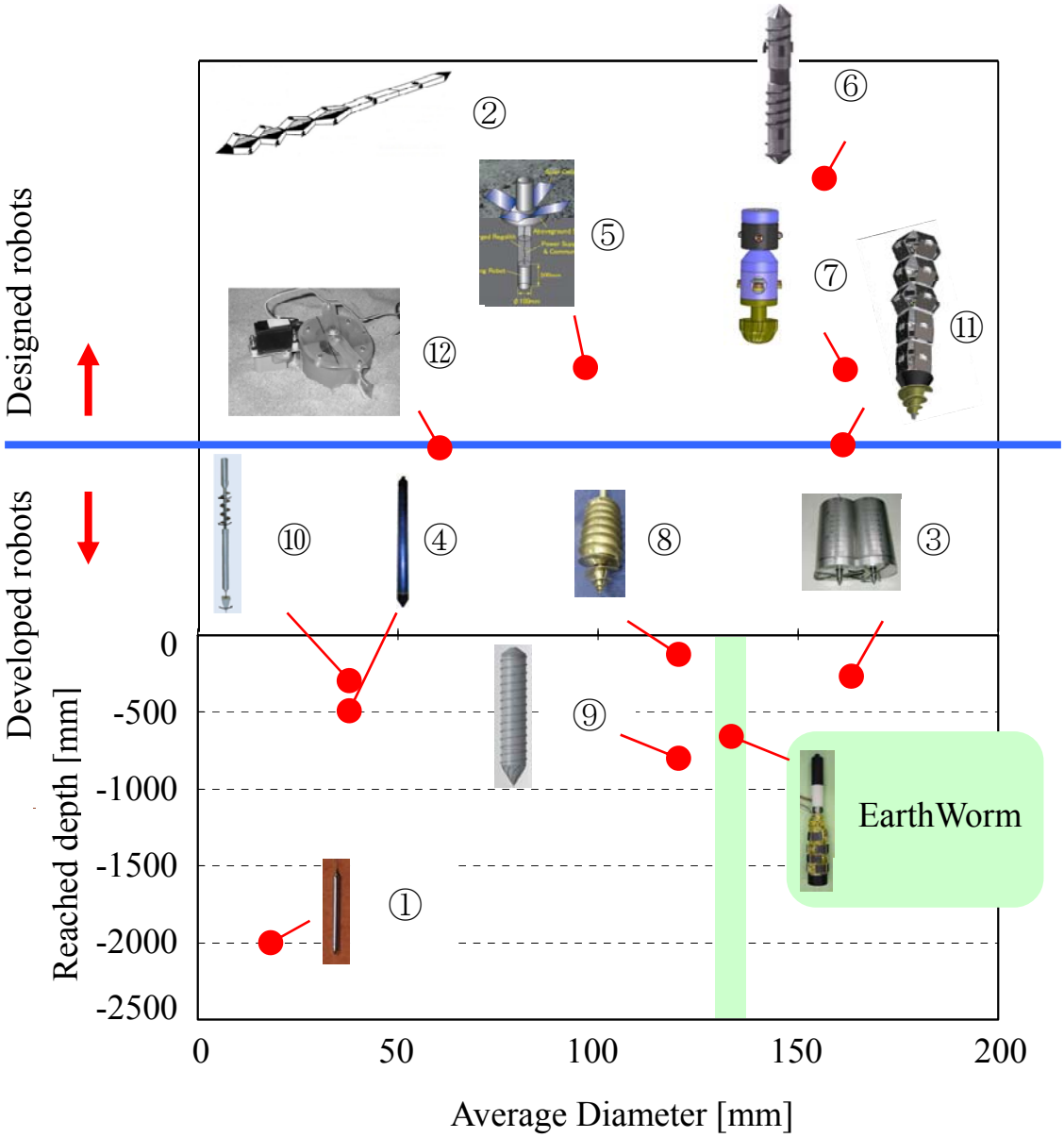

Fig. 2.24 Depth reached by various robots [32]

2.3.2 Effect of the Earth Pressure for Propulsion

The soil retaining wall is affected by the lateral earth pressure. Here, this earth pressure working around the body of an excavator is calculated using Coulomb theory. Fig. 2.25 shows the two conditions while the excavator moving downward inside the excavated hole. First, the excavator starts excavating and keeping contact with the wall of the hole (a). Then, its whole body is beneath the surface level (b). The normal stress σ_Z at a depth z is given as follows:

$$\sigma_Z = \gamma_Z z \tag{2.1}$$

Here, γ_Z is the density of a soil.

The horizontal stress σ_a is given in (2.2) using coefficient of earth pressure.

$$\sigma_a = K\sigma_Z \tag{2.2}$$

This stress works around the cylinder shape of the excavator and prevents from moving downward in the end. Then the resistance force F_1 and F_2 are expressed as follows:

$$\begin{cases} F_1 = \mu A \int_0^{H_{F1}} \sigma_a dz & (0 \le H_{F1} < H_L) \quad (2.3) \\ F_2 = \mu A \int_{H_{R2}}^{H_{F2}} \sigma_a dz & (H_L \le H_{F2}) \quad (2.4) \end{cases}$$

Here, H_L is the length of the excavator and A is the surface area between the excavator and the hole. When the excavator stops moving downward, the resistance force (F_1 or F_2) and weight of the excavator (W) equals each other. Therefore, the resistance force can be replaced with weight W in the equations (2.3) and (2.4). The depth of the excavator is given by these equations.

$$\begin{cases} H_{F_1} = (\frac{W}{Q_1 D})^{\frac{1}{3}} & (0 \le H_{F1} < H_L) \quad (2.5) \\ H_{F_2} = \frac{1}{2H_L^2}(H_L^3 + \frac{W}{Q_1 D}) & (H_L \le H_{F2}) \quad (2.6) \end{cases}$$

$$Q_1 = \frac{1}{2}\pi K \gamma_Z \mu \tag{2.7}$$

Here, D is the diameter of the excavator and μ is the coefficient of friction between the excavator and the hole.

Fig. 2.26 shows depth prediction from the equations (2.5) − (2.7). The parameters for calculation are shown in Table 2.2. Three figures illustrate the different length of the excavator. The horizontal

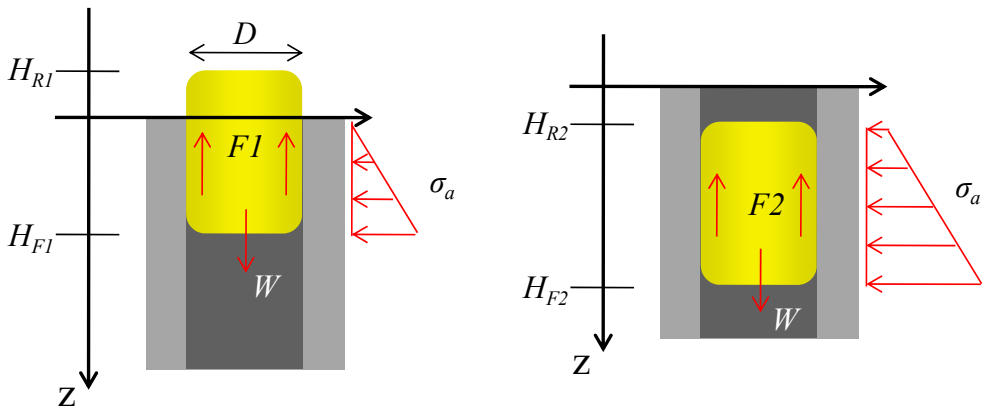

a) Before burying a whole body b) After burying a whole body

Fig. 2.25 Depth prediction by earth pressure

axis is the diameter of the excavator and the vertical is the reached depth of an excavator. Each figure has four plots showing different weights of excavator from 10 to 40 N every 10 N. Seen these results, the excavator is required to have short diameter and length, heavy body to excavate to a deep depth.

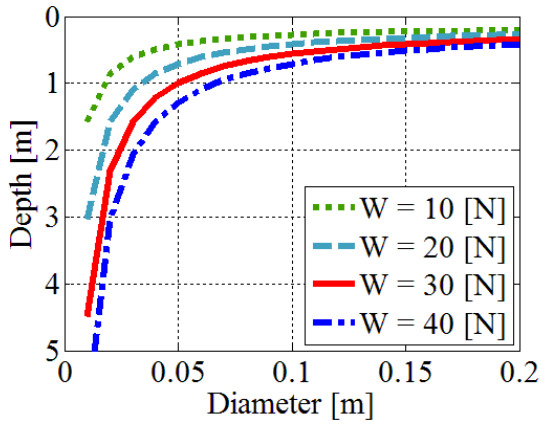

a) H_L = 0.25 [m]

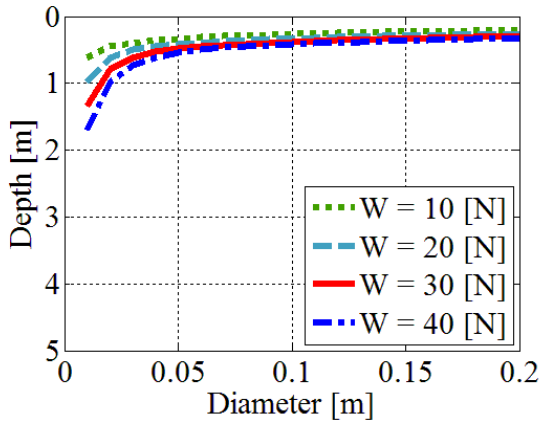

b) H_L = 0.50 [m]

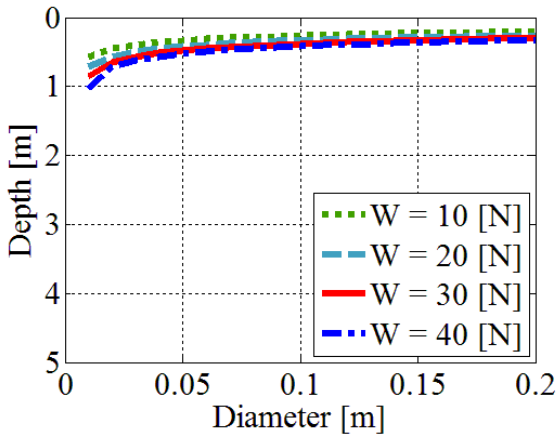

c) H_L = 0.75 [m]

Fig. 2.26 Depth prediction against the diameter and the weight of an excavator

Table 2.2 Parameters for depth prediction model

D [m]	Diameter	0.01 − 0.20
K	Coefficient of earth pressure	0.5
W [N]	Weight	10 − 40
γ_Z	Density	10.78×10^3
μ	Coefficient of friction between soil and excavator	0.65

2.3.3 Novel Concept for Excavator

From Fig. 2.24, it can be inferred that as the excavator becomes larger, it is more difficult to excavate deep into the soil. It is also described in Section 2.3.2 that the earth pressure acting on the outer surface of an excavator increases as the excavator excavates deep. First important task is to surely make a space for propulsion of the robot. It's not easy to push the front soil to the side. The outside transport is one of the solutions though the transported soil keeps contact with the soil around. The transport resistance would increase with the excavation depth. Therefore, the inside transport would be a solution to large diameter excavator. The mechanism to move forward plays an important role and is a challenging part. The friction around it increases and prevents it from tunneling deep [42] with the hammering mechanism, using own mass, pushing rear soil, screw and paddle. The wheel mechanism would effectively work in hard material such as a rock but the wall of the regolith would collapse and a robot would stop excavating. Hence, this paper focus on a subsurface explorer robot that features both propulsion and excavation units. The developed excavator design, which has a size sufficient to carry a seismometer and in situ scientific investigation devices, will appear within the green area in Fig. 2.24. The propulsion unit is based on the peristaltic crawling of earthworm and excavation unit is based on an earth auger (EA). The EA makes a space and transport the soil to the rear passing through inside the robot. The propulsion mechanisms of an earthworm and inchworm type are different. The inchworm mechanism consists of at least three units of two different types: one in front and rear for sustaining the robot with expanding in a radial direction and the other for contracting and extending in between the two units. What is more, the number of units became five if the three unit robot is added more units for the reason mentioned. While the earthworm mechanism requires at least three same type of unit, each unit can expand and contract in a radial direction and contract and extend in an axial direction, which enables to add the minimum number of one unit to the three unit robot. Furthermore, it could move with different propulsion patterns with only three units. Peristaltic crawling motion provides stability because the contracted body maintains contact with a large area of the surroundings, while the extending body from contracted is prevented from contact. The excavator is expected to decrease the blocking force for propelling deeper while maintaining the body position and orientation so that the excavation unit is not rotated. This arrangement should be able to excavate to deep depths.

Chapter 3: Peristaltic Crawling of an Earthworm

3.1 Mechanism of the Peristaltic Crawling

The inner structure of an earthworm is shown in Fig. 3.1 [65]. The earthworm consists of numerous segments divided by septa and a coelom containing the alimentary canal and nerve circuits. The inner wall of the body is composed of two muscle layers. The outside layer is called the circular muscle and the inside one is called the longitudinal muscle. When the circular muscle is actuated in a radial direction, the segment becomes thinner and extends in the axial direction. When the longitudinal muscle contracts in the axial direction, the segment gets thicker and shorter [66]. As a propulsion mechanism, an actual earthworm moves by peristaltic crawling. Fig. 3.2 shows the locomotion pattern of an earthworm during peristaltic crawling. First, the earthworm contracts its anterior segments. This increases the friction between the segments and the surrounding surface, as the thicker segments are in contact with the surface during locomotion. This friction generates a reaction force to extend the front contracted segments in the desired direction. The contraction propagates continuously toward the rear. This movement pulls the rear

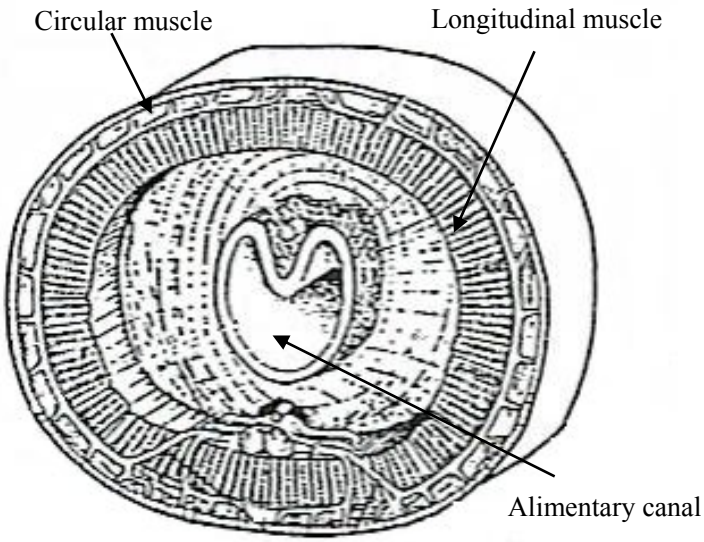

Fig. 3.1 Inner structure of an earthworm [65]

segments in the direction of movement. After the contraction is completed, the anterior segments of the earthworm are extended in the axial direction. There, each segment gets thicker in contracted mode, and thinner in extended mode during motion. This kind of locomotion is suitable for moving in perforated soil and is expected to provide stability in the underground, because the contracted body maintains contact with a large area of the surrounding soil, while the extended body is prevented from having contact to walls. This mechanism is therefore suitable for subsurface explorers.

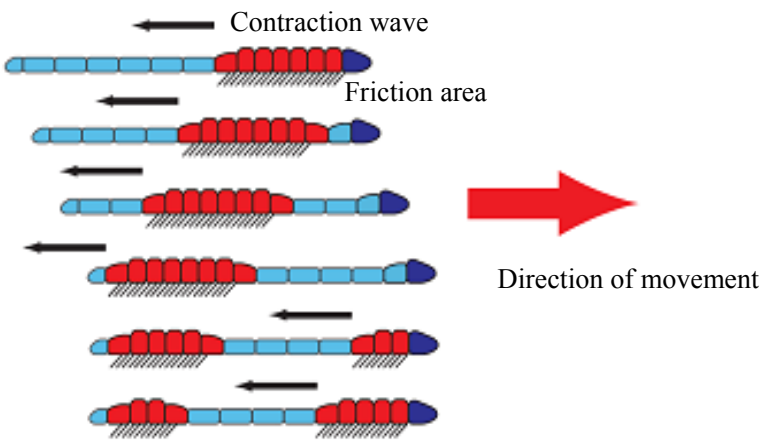

Fig. 3.2 Pattern of earthworm locomotion with peristaltic crawling

3.2 Measurement of an Actual Earthworm's Peristaltic Crawling

Motion of a real earthworm has been observed, known as naturally expert at underground mining, and transposed its behavior on the robot. A 140–150-mm-long and 4–6-mm-thick earthworm was

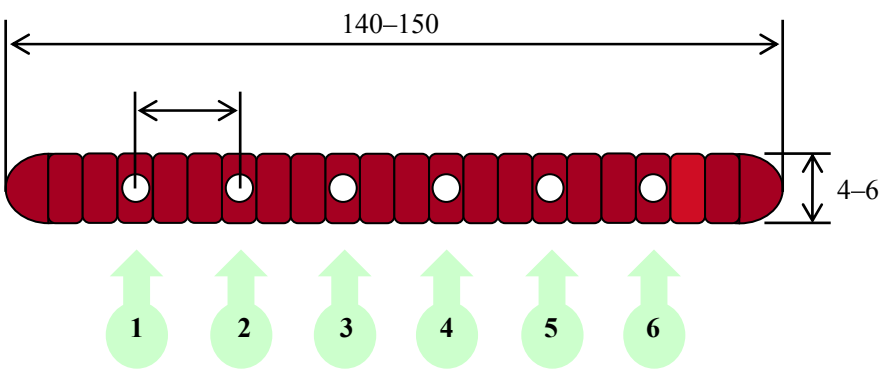

Fig. 3.3 Earthworm segments and markers

used. Markers were placed on the earthworm's segments every 19–25 mm (see Fig. 3.2). The locomotion was videotaped with a digital video camera and analyzed using a motion analysis software (MOVIAS Pro: Nac Image Technology Inc., Tokyo, Japan). The results obtained are shown in Fig. 3.4. This figure shows that the anterior part moves forward, then the posterior part moves forward along with the anterior part. Therefore, the contraction begins from the anterior part of the earthworm and continuously propagates toward the posterior part. The anterior segments contract again after propagation to the posterior part is complete. The average velocity of the earthworm was 16.1 mm/s. The peristaltic crawling robot was designed by taking these results into consideration.

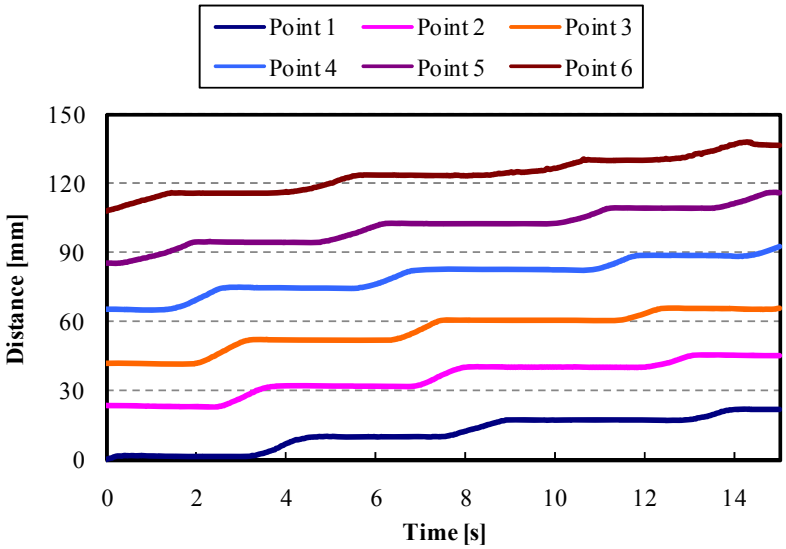

Fig. 3.4 Peristaltic crawling motion of the actual earthworm

Chapter 4: Concept of a Novel Subsurface Explorer Robot

4.1 Mechanism of a Novel Subsurface Explorer Robot

This section explains the concept of our underground explorer robot. The robot consists of two elements: a propulsion unit and an excavation unit (see Fig. 4.1). The peristaltic crawling behavior of an earthworm is adopted as the motion principle for the propulsion unit, and an earth auger (EA) is chosen as an excavation tool. The propulsion unit of the robot consists of four subunits corresponding to the individual segments of an earthworm. Fig. 4.2 shows their functioning while performing a peristaltic motion. Each subunit can contract and extend in the axial direction, and expand in the radial direction while contracting in the axial direction, thereby ensuring a high degree of friction between the body of the robot and its surroundings. Conversely, units that are extended in the axial direction do not make contact with their surroundings. The excavation unit of a prototype robot includes an EA with three parts allowing the following specific duties: excavation, transport, and discharge. The EA digs the hole, the front part excavates the material, and the screw part transports the excavated material to the rear of the EA. The robot excavates underground by making full use of these mechanisms.

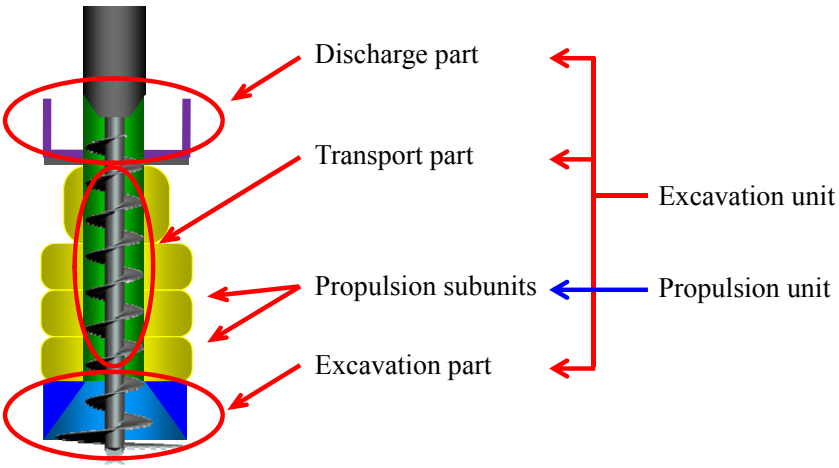

Fig. 4.1 Concept of the robot

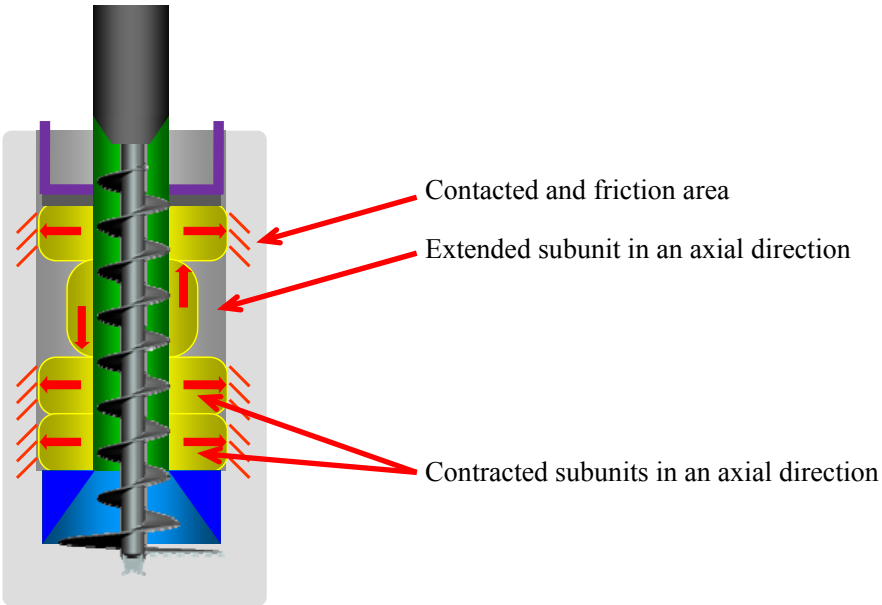

Fig. 4.2 Functioning of propulsion subunits inside a hole.

4.2 Excavation Motion in Future Missions

Fig. 4.3 illustrates the beginning of the mission using a rover, a launcher and the robot. The process is explained as follows:

1) The rover on the surface of the Moon drives to a spot for underground exploration and sets the launcher.
2) The launcher expands the solar panel that supplies the electricity to the excavation system and firmly fixes the launcher to the surface.
3) The robot is mounted inside the launcher and sustains the position with contracting the all propulsion subunits. Then it starts excavating using the propulsion and excavation units.

Fig. 4.4 details the motions involved in implementing the excavation process. There are 4 phases:

1) Each contracted subunit maintains contact with the wall of the hole, maintaining its body position and orientation, thereby coping with the perturbations induced by the rotating action of the excavating EA. At the same time, the EA excavates material in front of the robot. The second and third subunits from the front contract and sustain their positions. The front subunit extends to the front because the second and third subunits sustain their positions, and the extension force is applied in a downward direction, while the rear subunit contracts, permitting the robot to effectively move downward.

2-4) Extension propagates toward the rear, and the spiral of the EA (the transport component) carries excavated material to the rear of the unit, where it is discharged in a bucket.

The same amount of material is discharged at the rear end of the robot as is excavated from its front end; however, the volume of excavated material is much larger than that of the packed material in front of the robot. Therefore, the robot equips with the discharging part to carry material on the surface. Fig. 4.5 details the discharging process using a bucket.

a) The robot repeats phases 1–4 to excavate its way underground. Then the bucket is filled with the discharged material.

b) The bucket is lifted to transport and discharge to the surface. The material is discharged and the bucket becomes empty.

c) The empty bucket returns to the end of the robot. The robot is able to restart the excavation process again.

The excavation robot repeats phases 1–4 to excavate its way underground. The front unit contracts in the radial direction, and thus does not generate friction with the wall of the hole, when the robot moves downward as a result of performing phase 4–1. Thus, the robot decreases the effect of friction that traditionally limits propulsion.

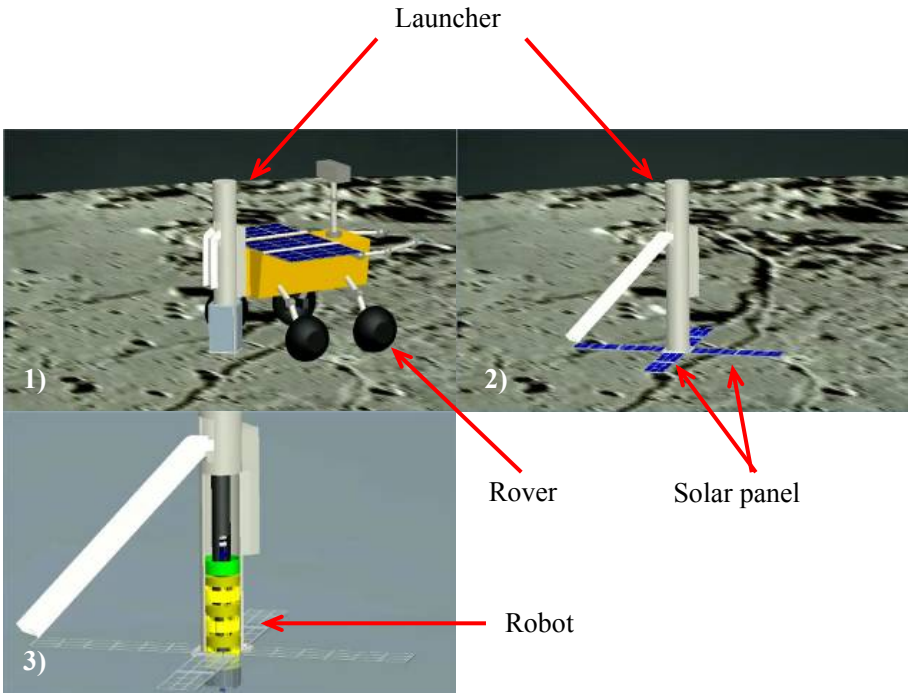

Fig. 4.3 Beginning of the mission

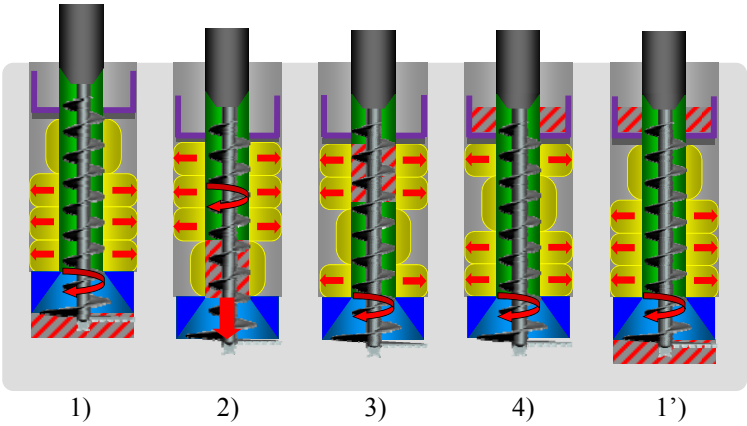

Fig. 4.4 Motions of excavation with the propulsion and excavation units

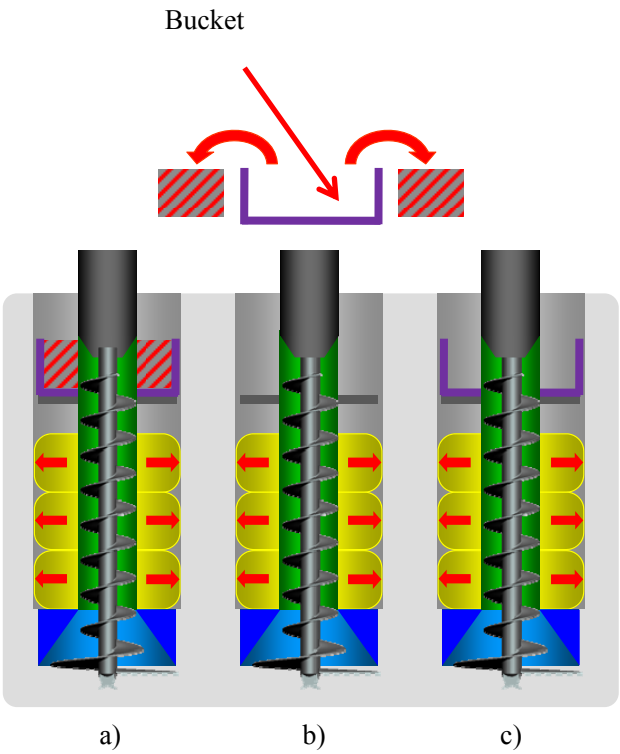

Fig. 4.5 Discharging process of the robot

Chapter 5: Development of an Excavation Unit

An excavation unit has been developed to be later combined with the propulsion unit. Several excavation experiments were carried out with the excavation unit alone to examine the effect of friction with the walls of the hole, to estimate possible excavation depth, and to obtain realistic requirements for the propulsion unit.

5.1 Development of Tapering Earth Auger

The excavation part of the proposed robot excavates a hole with the same diameter as the propulsion unit, thus allowing the robot to advance. In addition, the excavated soil is carried through the propulsion unit by the turning of the EA. Therefore, the diameter of the EA must narrow down between the excavation part and the transport part. An auger that has been developed tapers in diameter by using the fishtail single-spiral type [67]–[69]. Fig. 5.1 and 5.2 show the characteristics and specifications of the excavation unit. The front pitch P_f is shorter than P_r to decrease the amount of excavated soil that gets stuck because of the narrowing of the auger. Since peristaltic crawling

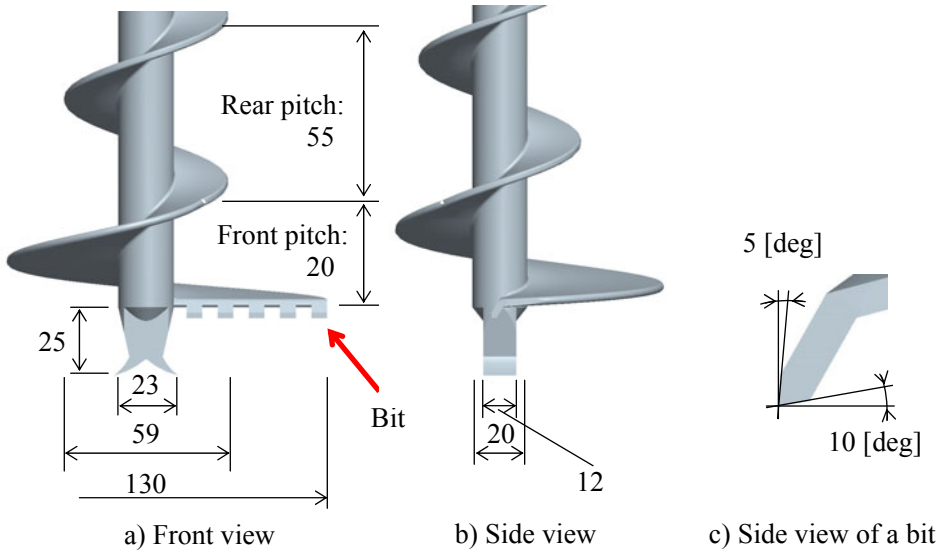

Fig. 5.1 Dimension of EA ([mm])

requires at least three rings (subunits), it is considered useful for this robot to have four units, thus providing enough force. Then the robot is able to move with several propulsion patterns, and it can sustain its position with at most two contracted units. The EA is 538 mm long, which is longer than the combined four units used for peristaltic crawling taking into account a length of discharge part.

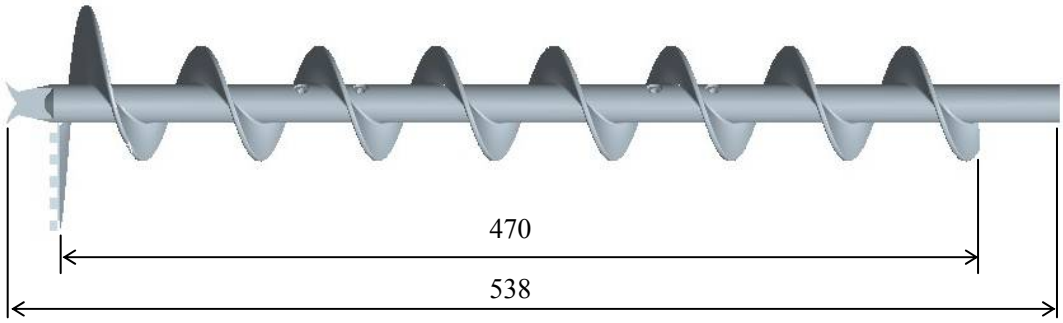

Fig. 5.2 Dimension of a whole EA ([mm])

5.2 Tracks of Tapering EA

Frist, tracks on the edge of the tapering EA is calculated before the volume calculation contained inside the EA. The pitch from the front gradually changes to the rear to smooth its difference between the front and rear. Note that the pitches are considered as constant, only the front pitch and the rear, to simplify calculations. Archimedean helix is expressed with the orthogonal coordinate as follows with the parameter θ that represents the angle of rotation.

$$x = a\cos\theta \tag{5.1}$$

$$y = a\sin\theta \tag{5.2}$$

$$z = b\theta \tag{5.3}$$

The parameters a and b are arbitrary variables. This helix is also expressed with the polar coordinates as follows:

$$r = a \tag{5.4}$$

$$z = b\theta \tag{5.5}$$

Fig. 5.3 shows the example of Archimedean helix in the orthogonal coordinate system. The detail parameters of the helix are written in the figure.

Fig. 5.4 shows the variable numbers of the tapering EA to calculate the tracks and volume. The track on the edge is defined as $P(r, \theta, z)$: r is the radius, θ is the angle that starts from x axis, z is the height of the track. P_0 is the starting point, P_1 is the end point of tapering, P_2 is the point rotated at PI (one rotation from the P_1), P_{end} is the end point of screw part.

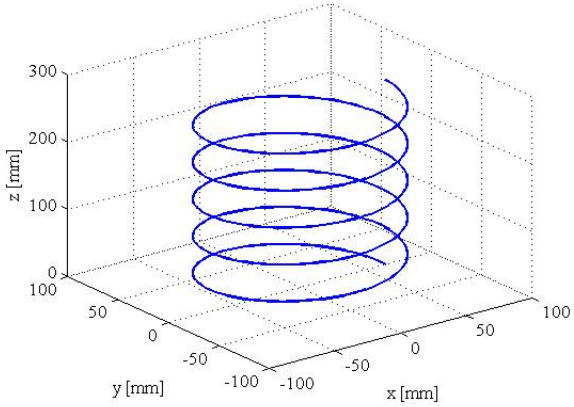

Fig. 5.3 Example of Archimedean helix

(a = 65, b = 8.75, 0 <= θ <= 31.4)

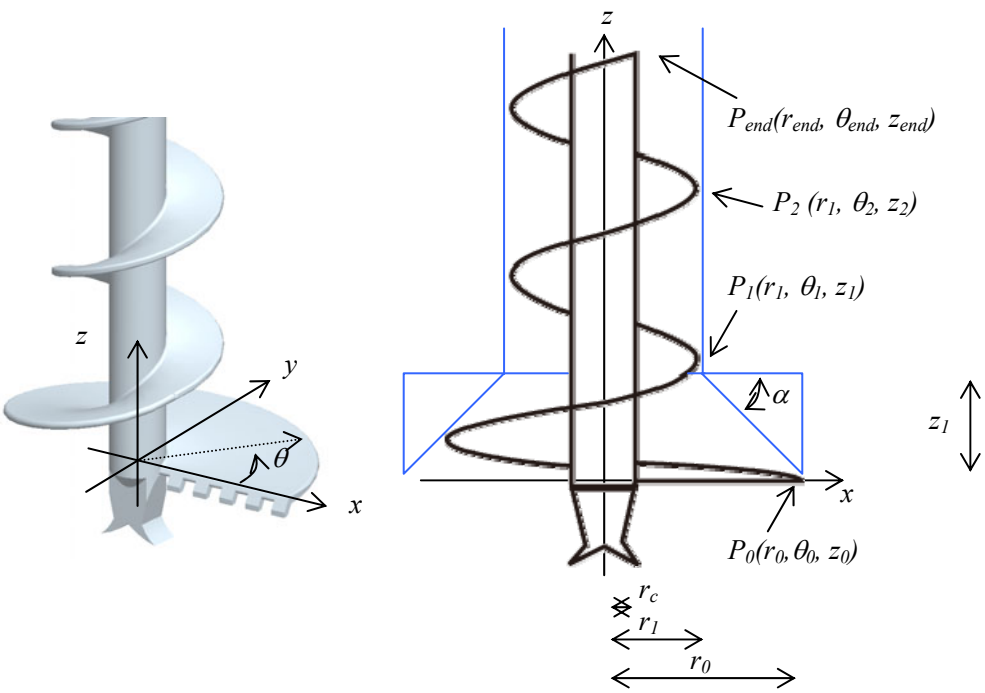

Fig. 5.4 Variable numbers of the tapering EA

The track is calculated with dividing into two: inside the tapering and after tapering EA.

i) Inside tapering EA (0 <= θ < θ_1)

Fig. 5.5 shows the parameter r inside the tapering EA. This is simply showed as the subtraction of tapering part. Parameters of the polar coordinates are expressed as follows:

$$r = a_1 \tag{5.6}$$

$$z = b_1\theta \tag{5.7}$$

$$a_1 = r_0 - b_1\theta \tan(\frac{\pi}{2} - \alpha) \tag{5.8}$$

$$b_1 = \frac{z_1}{\theta_1} \tag{5.9}$$

$$z_1 = (r_0 - r_1)\cot(\frac{\pi}{2} - \alpha) \tag{5.10}$$

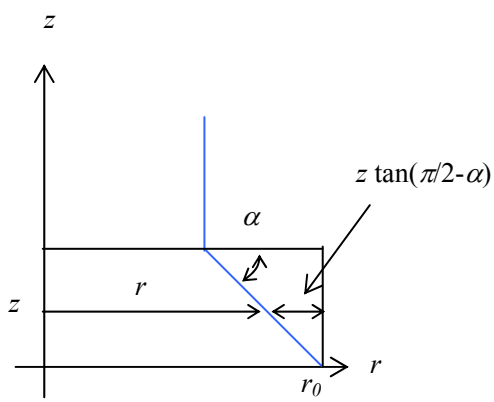

Fig. 5.5 Parameters of tapering EA

ii) Non-Tapering EA ($\theta_1 <= \theta <= \theta_{end}$)

Pitch and radius are constant in this area. Therefore, radius r and height z are given as follows:

$$r = a_2 \tag{5.11}$$

$$z = z_1 + b_2(\theta - \theta_1) \tag{5.12}$$

$$a_2 = r_1 \tag{5.13}$$

$$b_2 = \frac{p_r}{2\pi} \tag{5.14}$$

The track is calculated using equation explained before. Table 5.1 is the parameters for calculation of EA and Fig. 5.6 shows the calculated results illustrated from different angles.

Table 5.1 Parameters for calculation

d [mm]	65	α [rad]	π / 4
b_1 [mm]	5.7	θ_1 [rad]	5.69
r_0 [mm]	65	θ_2 [rad]	17.64 * π

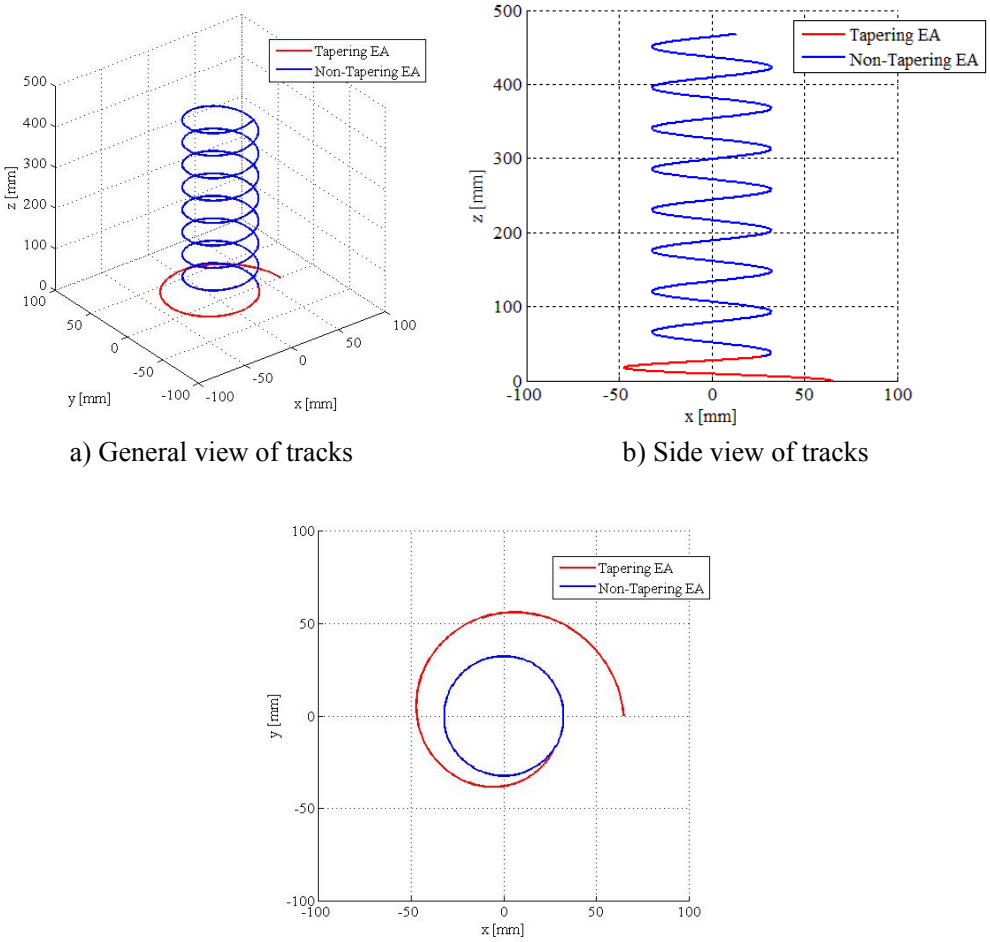

a) General view of tracks

b) Side view of tracks

c) Top view of tracks

Fig. 5.6 Calculated tracks

5.3 Volume of Soil inside EA

5.3.1 Volume Modeling of Soil inside EA

The volume of the soil fully contained inside the excavation part is calculated as shown in Fig. 5.7. The total volume which is omitted the EA part is illustrated in figure (a). In figure (b), it is divided into 3 parts. V_1 is the volume inside tapering part, V_2 is the soil above the tapering part from the beginning of the tapering EA to its end, V_3 is the volume of non-tapering EA. Therefore, the volume V is given as follows:

$$V = V_1 + V_2 + V_3 \tag{5.15}$$

i) Volume V_1 ($0 <= \theta < \theta_1$)

The volume of tapering part V_1 is a subtraction of the outside tapering part from the non-tapering part (Fig. 5.7 (c)). Here, the volume V_1 is given as follows:

$$V_1 = V_{11} - V_{12} \tag{5.16}$$

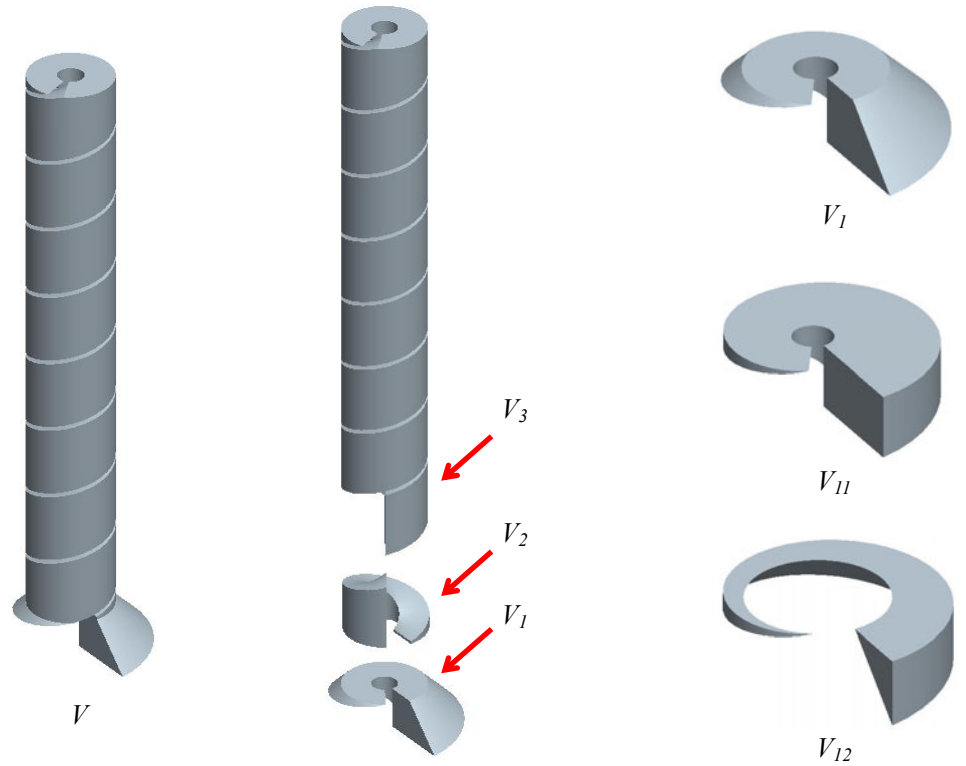

a) Total volume b) Divided volume c) Divided volume of V_1

Fig. 5.7 Volume calculation

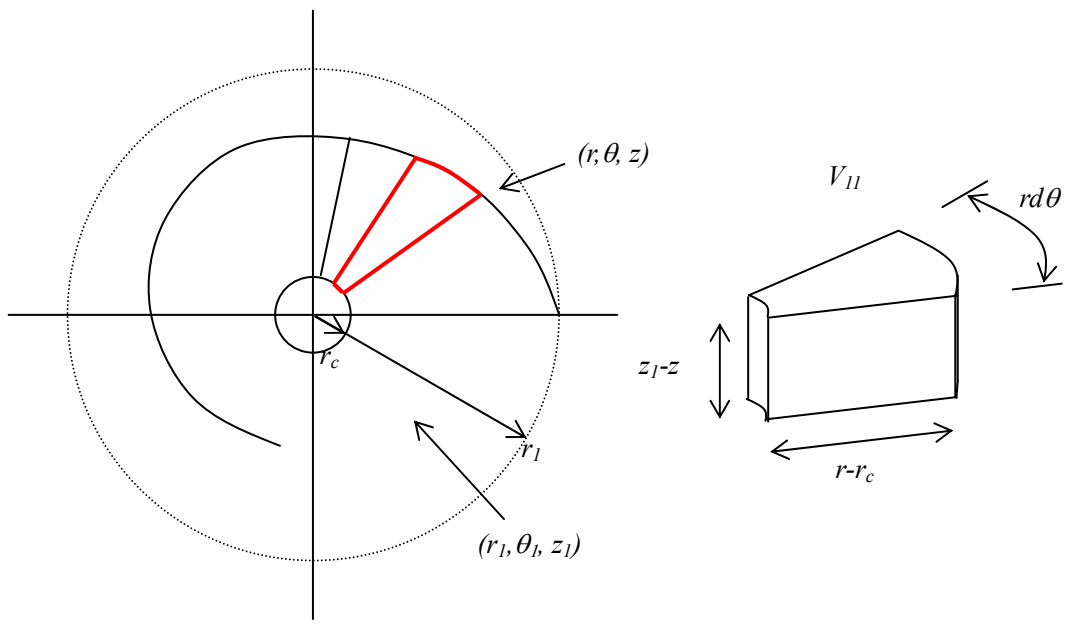

a) Top view of tapering EA b) Tiny volume

Fig. 5.8 Volume calculation V_{11}

Fig. 5.8 shows the calculation of volume V_{11} using integration. The red tiny area is at the arbitrary point (r, θ, z) in figure (a). The tiny volume in figure (b) corresponds to the red area in figure (a). The tiny volume dV_{11} is given as follows:

$$dV_{11} = \frac{1}{2}(r^2 - r_c^2)d\theta(z_1 - z) \tag{5.17}$$

dV_{11} is integrated by θ using the equations (5.6)–(5.9). Here, α is defined as $\pi/4$. Finally, the volume V_{11} is calculated including the parameters of (5.20).

$$V_{11} = \frac{1}{2}\int_{\theta_0}^{\theta_1}\left\{(r_0 - b_1\theta)^2 - r_c^2\right\}(z_1 - b_1\theta)d\theta \tag{5.18}$$

$$V_{11} = \frac{1}{2}\{A(\theta_1 - \theta_0)^4 + B(\theta_1 - \theta_0)^3 + C(\theta_1 - \theta_0)^2 + E(\theta_1 - \theta_0)\} \tag{5.19}$$

$$\begin{cases} A = -\frac{1}{4}(b_1^3) \\ B = \frac{1}{3}(2r_0 b_1^2 + g^2 z_1) \\ C = \frac{1}{2}(r_c^2 b_1 - r_0^2 b_1 - 2r_0 b_1 z_1) \\ E = (r_0^2 - r_c^2)z_1 \\ g = b_1 \tan(\frac{\pi}{4}) \end{cases} \tag{5.20}$$

Fig. 5.9 shows the intersection of the volume V_{12}. This area is a simple triangle. The width is on the arc at the gravity point of the triangle. Therefore, the volume V_{12} is given in (5.22) and (5.23).

$$dV_{12} = \frac{1}{2}(r - r_1)(z_1 - z)\frac{2r + r_1}{3}d\theta \tag{5.21}$$

$$V_{12} = \frac{1}{36}\{F(\theta_1 - \theta_0)^4 + G(\theta_1 - \theta_0)^3 + H(\theta_1 - \theta_0)^2 + I(\theta_1 - \theta_0)\} \tag{5.22}$$

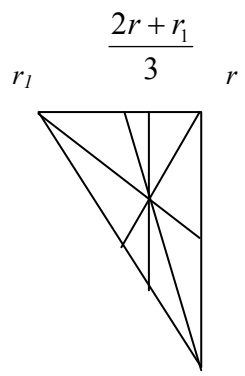

Fig. 5.9 Intersection of the volume V_{12}

$$\begin{cases} F = -\frac{1}{3}(b_1^3) \\ G = 2b_1^2(4r_0 - r_1 + 2z_1) \\ H = 3b_1(-2r_0^2 + r_0(r_1 - 4z_1) + r_1(r_1 + z_1)) \\ I = 6(r_0 - r_1)(2r_0 + r_1)z_1 \end{cases} \tag{5.23}$$

ii) Volume V_2 ($0 <= \theta < \theta_1$)

Fig. 5.10 shows the calculation of volume V_2. It is given the equation (5.24) which is subtracted from the volume of the screw part.

$$V_2 = V_{21} - V_{22} + V_{23} \tag{5.24}$$

The tiny volume dV_{21} include the screw part is expressed in the equation (5.25). The volume is integrated using the equations of (5.27) and (5.12).

$$dV_{21} = \frac{1}{2}(2\pi r + l_2)(z - z_1)dr \tag{5.25}$$

$$l_2 = 2\pi r \frac{p_r - (z - z_1)}{p_r} \tag{5.27}$$

$$V_{21} = \int_{r_c}^{r_1} \frac{1}{2}(2\pi r + l_2)(z - z_1)dr \tag{5.28}$$

$$V_{21} = \frac{\pi}{2}(1 + \frac{P_r - (b_2(\theta - \theta_1))}{P_r})(b_2(\theta - \theta_1))(r_1^2 - r_c^2) \tag{5.29}$$

The screw part should be subtracted from the volume V_{21}. Its equation is given as follows:

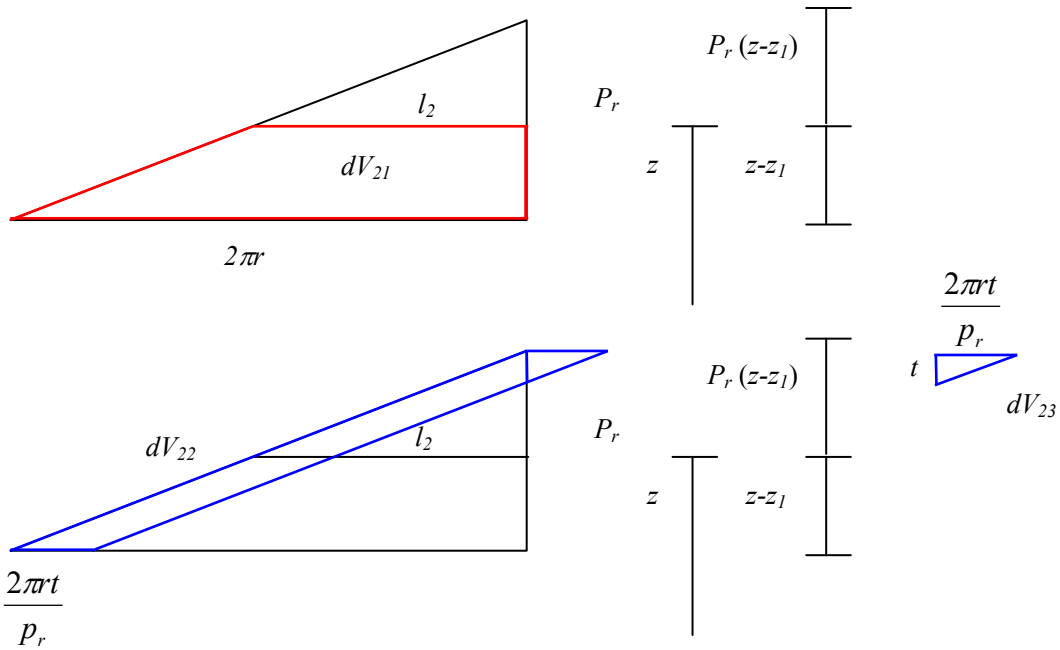

Fig. 5.10 Volume calculation V_2

$$dV_{22} = \frac{2\pi rt(z - z_1)}{p_r} dr \tag{5.30}$$

$$V_{22} = \frac{\pi t b_2(\theta - \theta_1)}{p_r}(r_1^2 - r_c^2) \tag{5.31}$$

The V_{21} has the space V_{23} that is not included in the V_2. Therefore, this volume V_{23} is required to add to the total volume V_2. The volume V_{23} is illustrated as a triangle in Fig. 5.10 and given as follows:

$$dV_{23} = \frac{\pi r t^2}{p_r} dr \tag{5.32}$$

$$V_{23} = \frac{\pi t^2}{2p_r}(r_1^2 - r_c^2) \tag{5.33}$$

iii) Volume V_3 ($\theta_1 <= \theta <= \theta_{end}$ and p_r <=//z//)

The V_3 is the space that is inside the non-tapering part is calculated as the equation (5.34). The soil is mainly classified into the part when the surface of the soil reaches the height of z (Fig. 5.11). The soil part of volume V_{31} is between the upper screw and lower. On the other hand, the soil part of volume V_{32} which shapes a triangle is not in between the two screws. Both volumes contain the volume of screw part V_{33}, so it is subtracted from them.

$$V_3 = V_{31} + V_{32} - V_{33} \tag{5.34}$$

The dV_{31} is given in the equation (5.35) using l_c expressed in (5.36).

$$dV_{31} = l_c p_r dr \tag{5.35}$$

$$l_c = 2\pi r \frac{(z - z_1) - p_r}{p_r} \tag{5.36}$$

The dV_{31} is integrated from the axis of the EA to the edge of screw. Then V_{31} is given in (5.38) using the equation (5.12).

$$V_{31} = \int_{r_c}^{r_1} l_c p_r dr \tag{5.37}$$

$$V_{31} = \pi\{b_2(\theta - \theta_1) - p_r\}(r_1^2 - r_c^2) \tag{5.38}$$

The dV_{32} has a simple triangle shape so it is integrated the same as the volume V_{31}.

$$dV_{32} = \pi p_r r dr \tag{5.39}$$

$$V_{32} = \pi p_r \frac{1}{2}(r_1^2 - r_c^2) \tag{5.40}$$

The screw part of dV_{33} is summed by a trapezium and a triangle shape (Fig. 5.12). Finally, V_{33} is integrated the same as before.

$$dV_{33} = l_c t dr + \frac{t^2}{p_r^2} V_{32} \tag{5.41}$$

$$V_{33} = \pi t \frac{(z - z_1) - p_r}{p_r}(r_1^2 - r_c^2) + \frac{t^2}{2p_r}\pi(r_1^2 - r_c^2) \qquad (5.42)$$

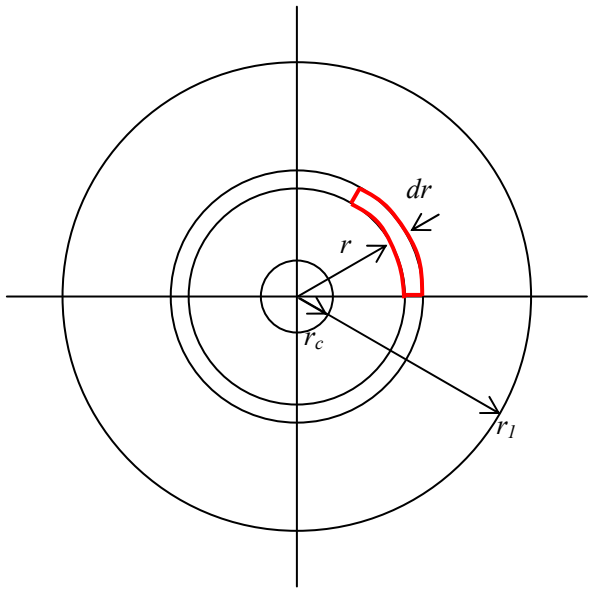

a) Top view of volume calculation V_3

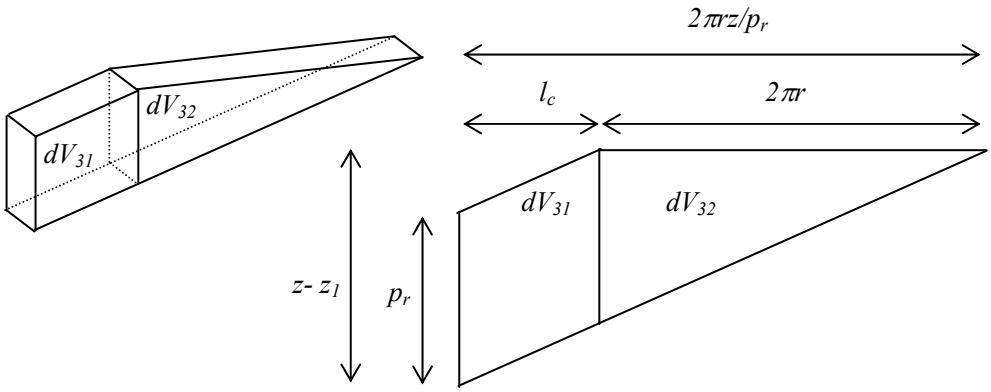

b) volume calculation V_{31} and V_{32}

Fig. 5.11 Volume calculation V_3

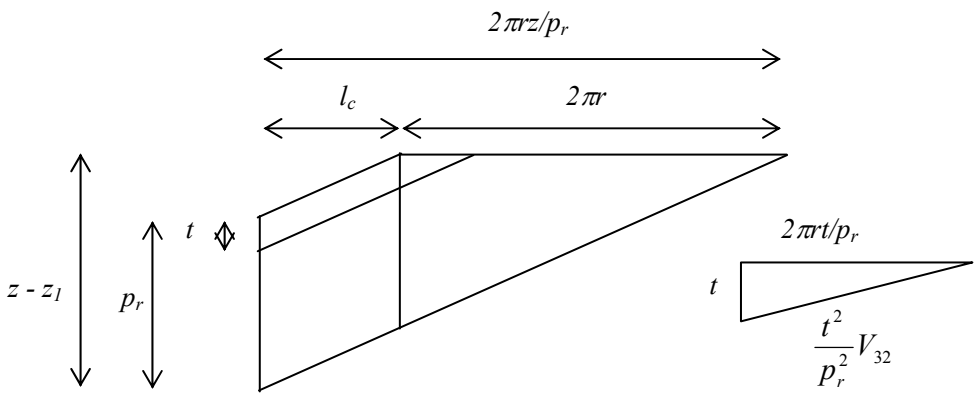

Fig. 5.12 Volume calculation V_{33}, screw part

5.3.2 Results of Calculation

The volume of soil inside the EA is calculated using the equations explained. Table 5.2 describes the parameters of EA for a calculation. Front and rear pitches are different from the developed EA explained in Section 5.1. As explained, the EA is designed using 3D-CAD, it enables to smoothly connect the changing point between tapering and non-tapering part, which results in smoothing the changing pitch. Instead of this, two unchanged pitches are used to simplify the calculation. Table 5.3 shows the results of each and total volumes.

Table 5.2 Detail parameters of EA

(r_0, θ_0, z_0)	(65, 0, 0)	α [rad]	$\pi / 4$
(r_1, θ_1, z_1)	(32.5, 5.70, 32.5)	t [mm]	3
$(r_{end}, \theta_{end}, z_{end})$	(32.5, 55.43, 470)	b_1 [mm]	5.7
p_f [mm]	35.8	r_c [mm]	10
p_r [mm]	55.3		

Table 5.3 Results of calculation ([mm^3])

V_{11}	133,892	V_{21}	83,065	V_{31}	1,150,826
V_{12}	48,897	V_{22}	9,008	V_{32}	83,215
V_1	84,995	V_{23}	277	V_{33}	62,404
		V_2	74,334	V_3	1,171,637
				V	1,330,966

5.4 Development of Excavation Unit

A DC motor (Maxon EC-Max 30, 60 Watt) controls the rotation of the EA (see Fig. 5.13). Inside, excavation support is used to cover the transport part. The excavation support also combines the skirt with the motor cover so that the skirt does not move under the influence of the EA and the excavated soil. Finally, the PVC plate covers the outside of excavation support to flatten out any possible irregularities. The total mass of the developed excavation unit is 5.9 kg.

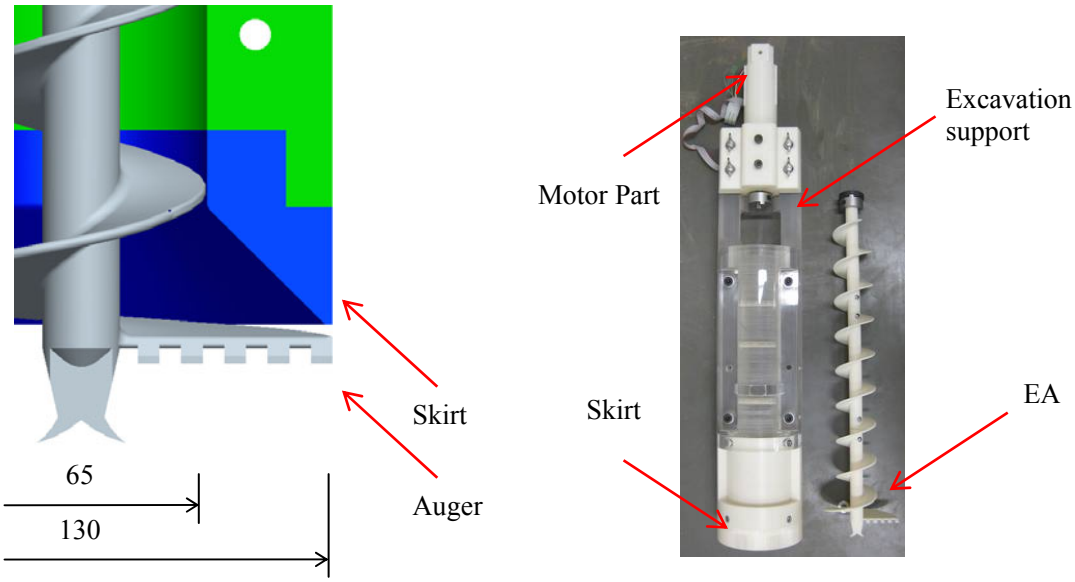

Fig. 5.13 Developed excavation unit

5.5 Excavation Experiment Setup

Fig. 5.14 shows the excavation experimental setup. The rear end of the motor part is fixed on the linear guides with a plate. The rotation of the excavation unit is reduced, and the excavation unit is able to excavate downward smoothly due to the linear guides. A counterweight is also fixed to the rear end of the motor part with a wire. The force pushing into the excavated soil is controllable at the beginning of the excavation experiments by changing the counterweight. This experiment measures the depth of excavation and motor torque while EA is excavating the reddish soil. The wire sensor measures the depth of excavation. Motor torque is obtained by the output current from the motor driver.

Fig. 5.15 shows the controlling system for the experiments. The controller (DES 50/5, Maxon) controls the motor for the EA. AD board (PCI 3153, Interface) collects analog data corresponding to a depth from the wire sensor (WDS-1000-C3-P, Micro-Epsilon). Inside the computer, a graphical user interface (DES User Interface, Maxon) controls the motor and C++ program controls the AD

board.

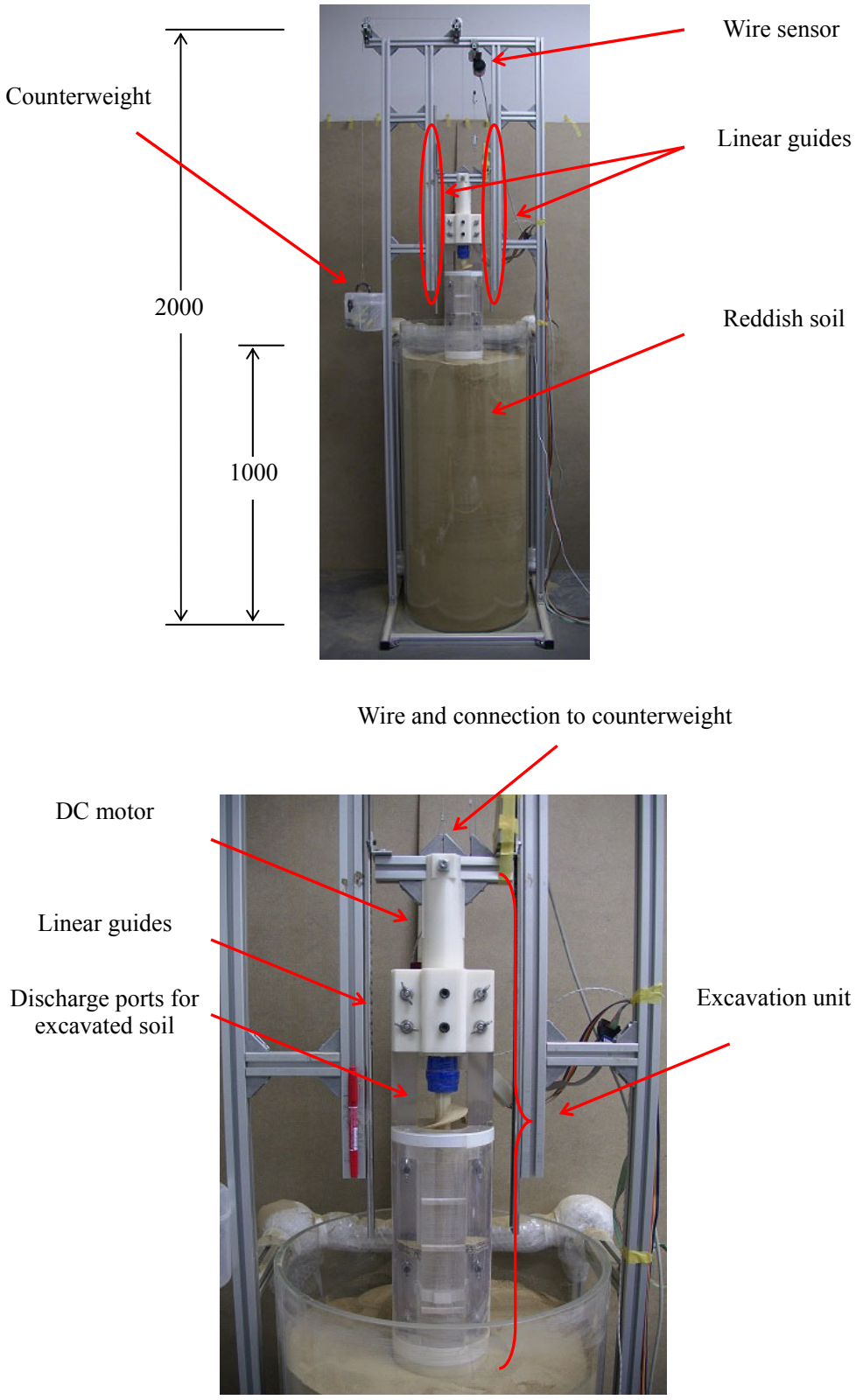

Fig. 5.14 Experimental setup

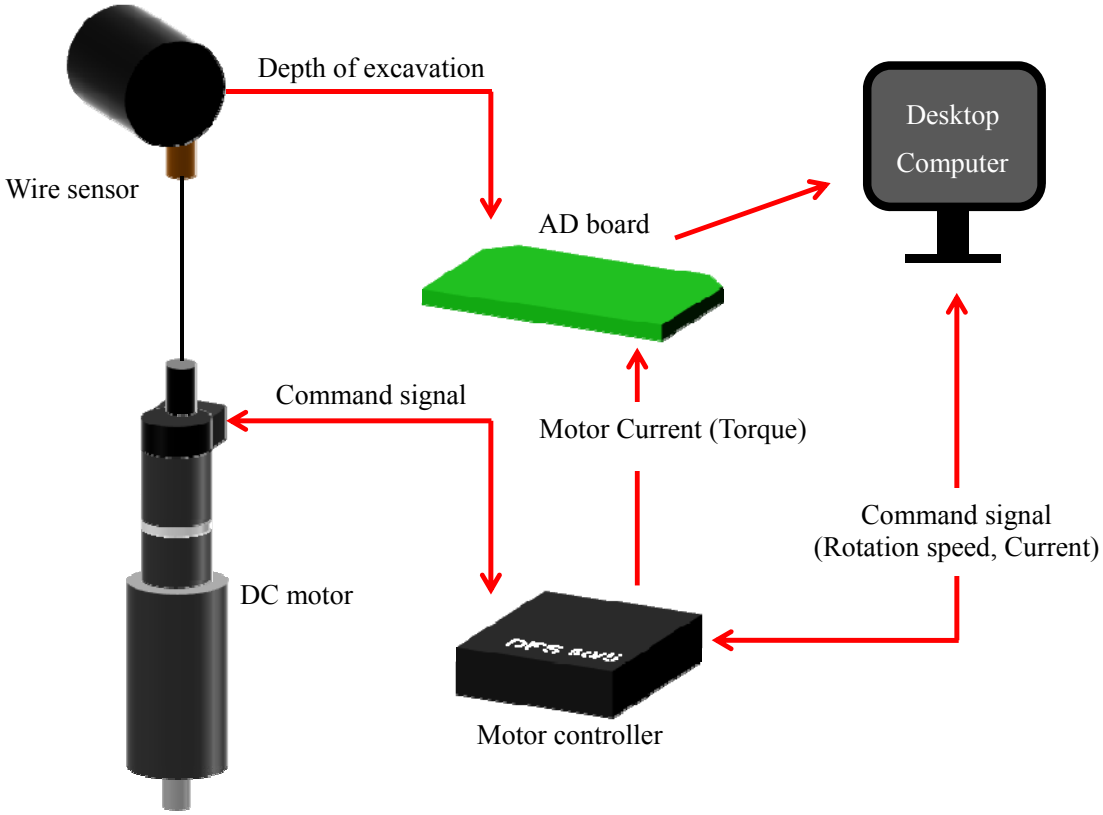

Fig. 5.15 Controlling system

A reddish soil is used for the excavation experiments. To compare its characteristics with lunar soil and a lunar simulant called Lunarlant, particle size distribution of the soils is used, which shows the size and range of the materials. Fig. 5.16 shows the particle size distribution of red soil, lunar soil [70]–[72] and Lunarlant [73]. W. David Carrier III [70] gathered the lunar soil data from some references of Apollo 11, 12, 14 and 15. Graf [71] gathered the data from some references of Apollo 11, 12, 14, 15, 16 and 17 and Luna 24. W. David Carrier III [72] again summarized the data of Graf [71] and added more data. The test was conducted to measure particle size distribution of the red soil according to the test method for particle size distribution of soils [74] specified by the Japanese Geotechnical Society. Some of regulations were also referred [75]–[79]. From the figure, the red soil shows the similar characteristic to the lunar soil but quantitative and qualitative comparison is needed. Therefore, the median diameter, uniformity coefficient and coefficient of curvature are used for validation. The median diameter D_{50} is the value of the particle diameter at 50% in the particle size distribution. The uniformity coefficient U_c, is the incline of the curvature, is given the following formula:

$$U_c = \frac{D_{60}}{D_{10}} \tag{5.43}$$

Here, D_{60} and D_{10} are values of 60% and 10% in the cumulative distribution.

The coefficient of curvature U_c', is shape and curvature parameter, is given the following formula:

$$U_c' = \frac{D_{30}^{\ 2}}{D_{10} D_{60}} \tag{5.44}$$

Here, D_{30} is value of 30% in the cumulative distribution.

Table 5.4 shows the three parameters mentioned of three materials. Reddish soil has similar characteristics to lunar soil but the average size of the particle is slightly smaller.

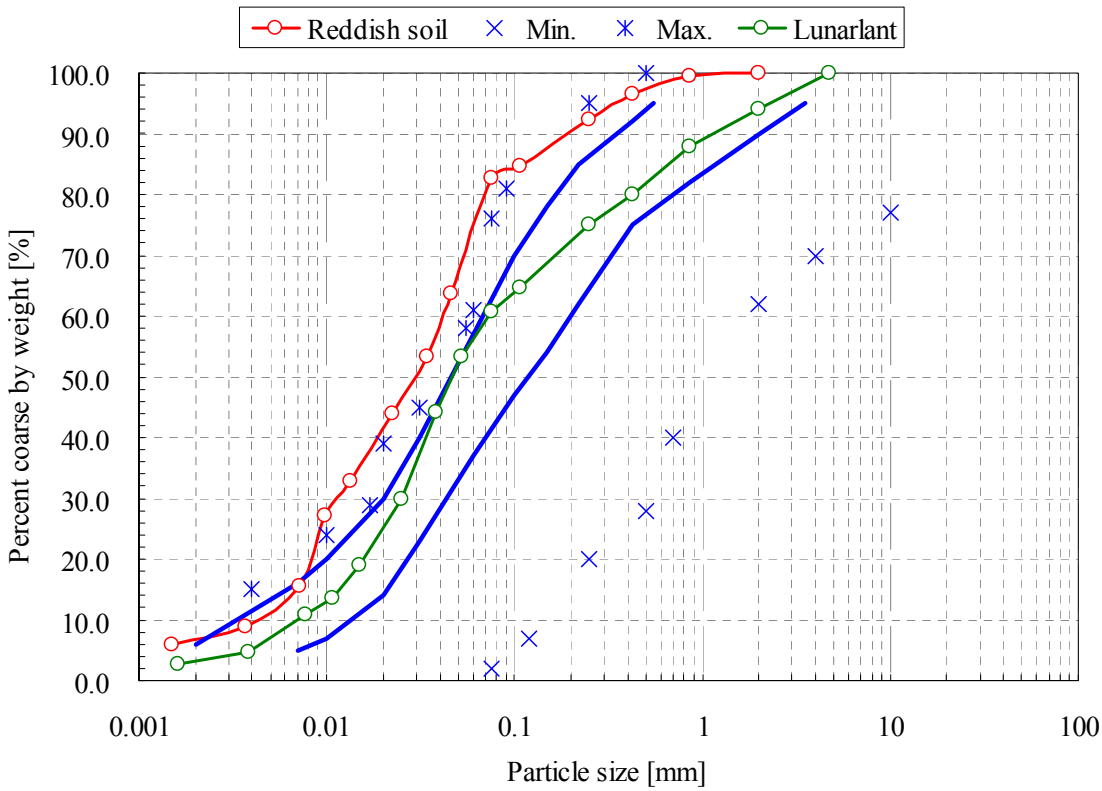

Fig. 5.16 Particle size distribution of lunar soil (lines: ±1 standard deviation from the average), reddish soil and Lunarlant.

Table 5.4 Comparisons of particle size parameters

		D_{50} [mm]	U_C	U_C'
Lunar soil	Av.	0.072	16	1.2
	Min.–Max	0.046–0.11	8.7–30	0.7–2.0
Red soil		0.030	9.5	1.0
Lunarlant		0.046	10	1.3

5.6 Excavation Experiments

As stated, the excavation unit is a separate unit and does not have a propulsion mechanism. While this unit is excavating, the friction from the surrounding environment increases and prevents the unit from excavating further. Thus, the excavation unit is not able to generate sufficient pushing force to continue digging. The depth of excavation is clearly related to the weight of the unit. To clarify this relationship, two types of excavation experiments are conducted. In the first experiment, the pushing force is changed, whereas in the second experiment, the speed of rotation is changed. In the pushing-force experiments, measured values are excavation depth and motor torque as functions of the pushing force. It is expected that the larger the pushing force is, the deeper the unit can dig because of the friction around the unit. The motor torque is also examined when the pushing force is the same as expected to be applied by the propulsion unit, in order to best prepare combinations of the excavation and propulsion units (see Chapter 6). In the rotation-speed experiments, the unit is expected to show that the excavation velocity changes when the rotation speed is increased. The depth of excavation should remain constant at any velocity because the pushing force is the same.

5.6.1 Changing the Pushing Force

In this experiment, the counterweight used to alter the pushing force was changed, and measured the depth of excavation and the current intensity corresponding to the motor torque. At the beginning of the experiments, the pushing forces were 52 N (weight of the robot including both the propulsion and the excavation units as described in Chapter 7), 26 N (1/2 of 52 N), 13 N (1/4 of 52 N), 55 N (extension force of a subunit, see Chapter 6), and the rotation speed was 10 r/min. Each experiment was conducted five times. Fig. 5.17 shows one of these experiments and the excavation unit excavating soil.

All the experiments were essentially similar in terms of functional result. Fig. 5.18 shows the depth of excavation and motor torque over elapsed time under the constraints of 10 r/min velocity and 52 N force. As seen, the excavation velocity was fast for the first 50 s and maintained at an almost

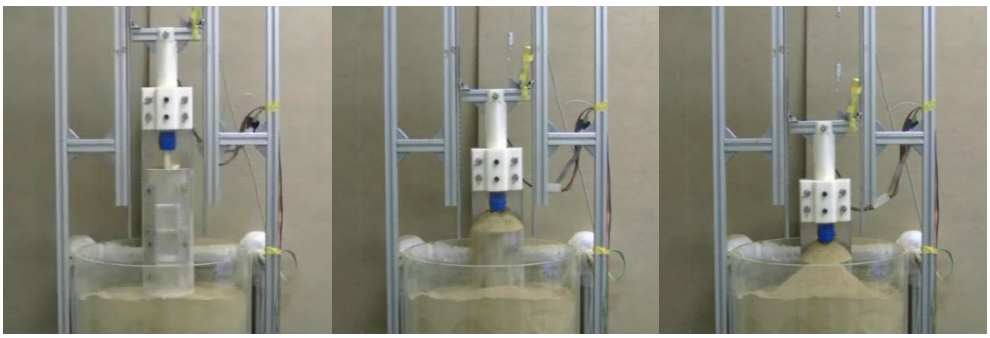

Fig. 5.17 Experimental results of developed excavation unit

constant average velocity until approximately 2.5 min, where it slowed to nearly zero shortly afterwards. The robot excavated to a depth of 219 mm. The motor torque increased for about 50 s, then gradually decreased.

Fig. 5.19 shows the effect of changing the pushing forces in four steps. Each bar on the left depicts the average reached depth of excavation of the five experiments and the bars on the right depict the average maximum excavation torque. Lines on the top of bars indicate the maximum and the minimum values. Fig. 5.20 shows the excavation velocity versus the pushing force. As seen in Fig. 5.19, the depth of excavation demonstrates a difference of about 100 mm between maximum and

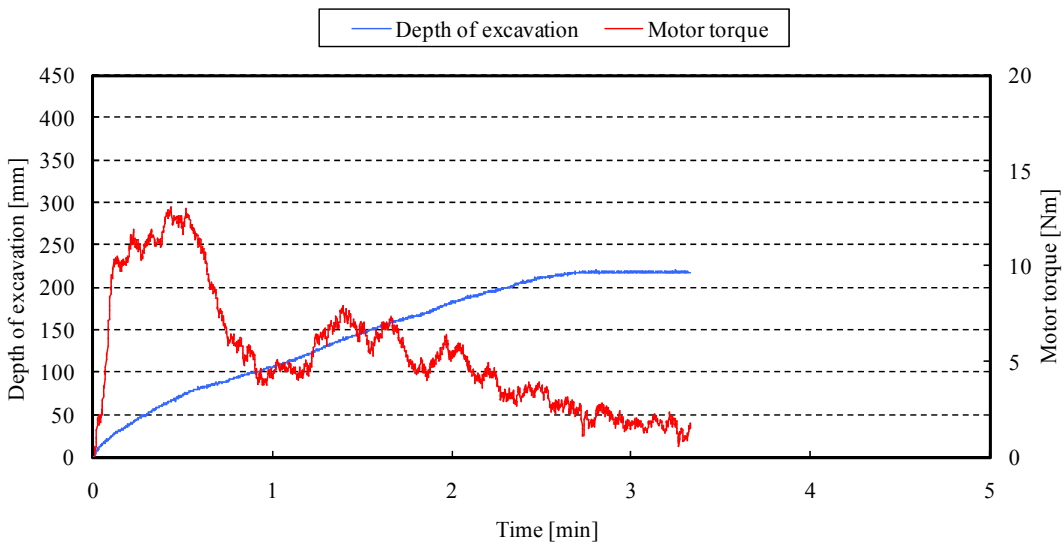

Fig. 5.18 Tracks of excavation (10 [r/min], 52 [N])

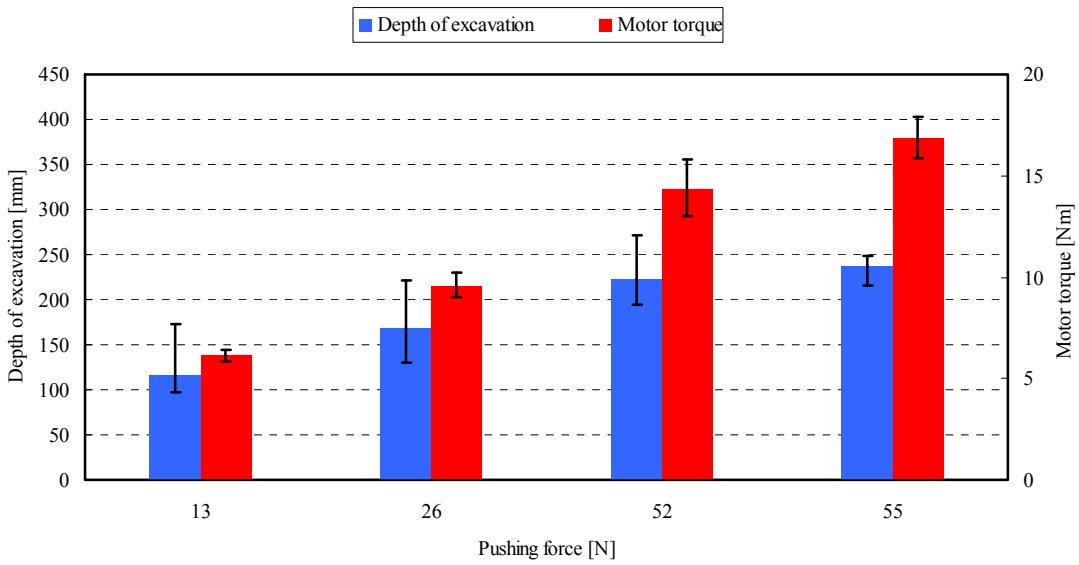

Fig. 5.19 Depth of excavation (left scale) and maximum motor torque (right scale) for different pushing forces (horizontal axis)

minimum, and the motor torque has a difference of about 3 Nm. These uncertainties are probably related to random variations in the soil. From these experimental results, it is concluded that both the depth of excavation and the motor torque rise in value when the pushing force is large, whereas the velocity slightly increases when the pushing force is increased.

The maximum motor torque shows about 18 Nm at 55 N of the pushing force, and the propulsion unit needs to maintain the body position orientation against this torque.

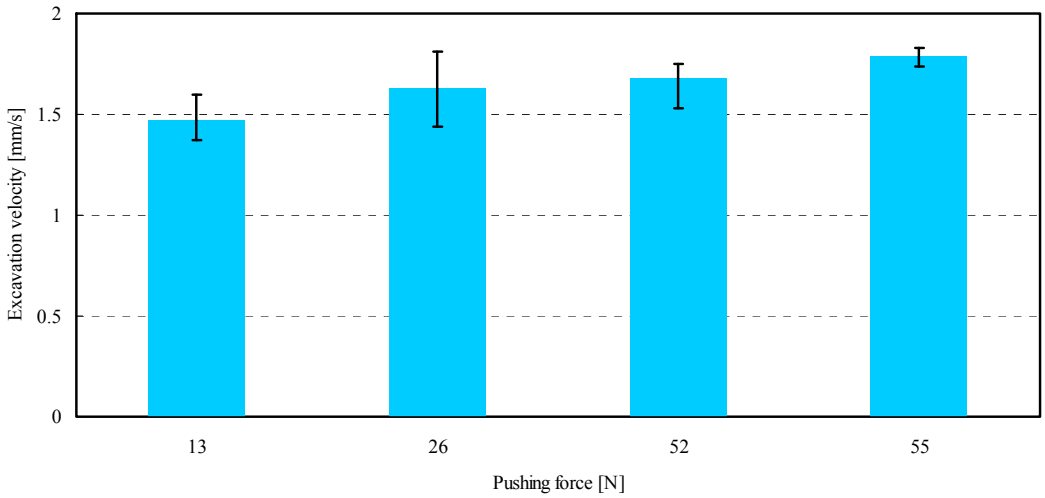

Fig. 5.20 Relationship between the pushing force and the excavation velocity

5.6.2 Changing Rotation Speeds

In this experiment, the rotation speed of EA was changed and measured the depth of excavation and the motor torque. The pushing force was set to 52 N, and the rotation speeds were 3, 5, and 10 r/min.

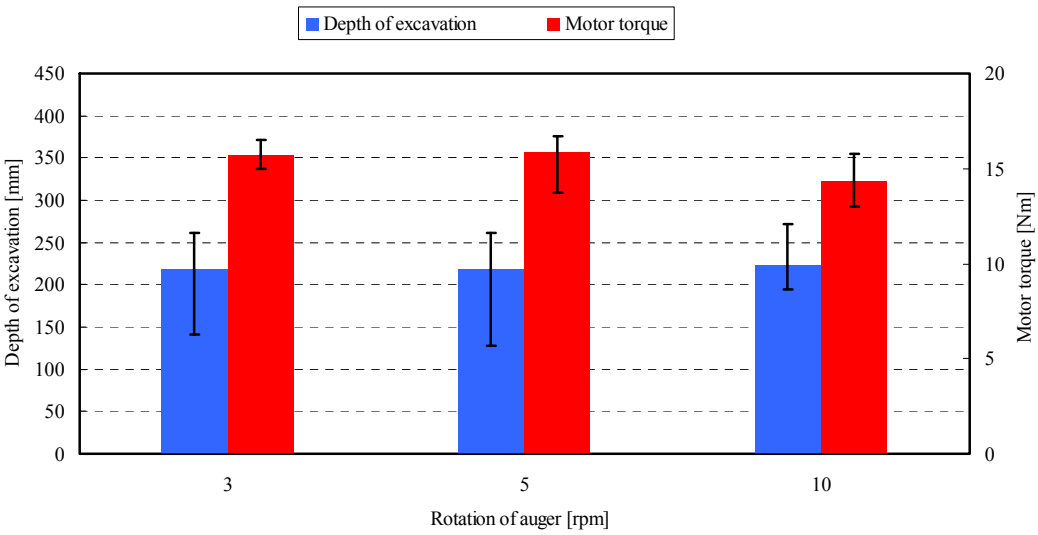

Fig. 5.21 Relationship between rotation speed and depth of excavation

Experimental results were obtained similar to those shown in Fig. 5.18. Fig. 5.21 shows the depth of excavation and the motor torque as functions of auger rotary speed. The depths reached were almost the same in the three cases. The required motor torque shows slight differences with the rotation speed. The maximum motor torque was measured as 15.7 Nm at 3 r/min. Fig. 5.22 shows the excavation velocity as proportional to the rotation of EA. The fastest velocity was 1.75 mm/s at 10 r/min. It was realized that when the EA rotates fast, it can excavate fast even though it is required to generate almost the same motor torque as when rotation is slow.

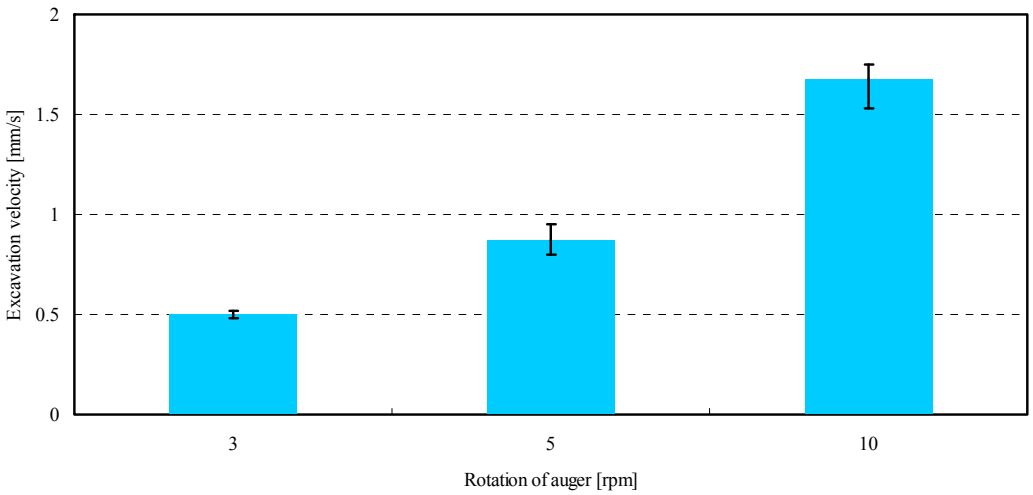

Fig. 5.22 Comparison of excavation velocities

5.6.3 Comparisons of the Effect of Earth Pressure and Experimental Results

The experimental results of the excavation unit were compared with the depth prediction equations (2.5)–(2.7). Table 5.5 shows the parameters of the propulsion unit and soil condition. Fig. 5.23 shows the comparisons of the model indicating the red plots and experimental results indicating the blue including error bars. The model qualitatively has similar results for the experiments but quantitatively has slightly different results. It is believed that the soil discharged from the discharge ports dropped into the tiny gaps between the excavated hole and the unit, then the friction increased between them, which results in the shallower excavation depth than the model. It is concluded that the earth pressure from the wall of the hole largely prevents the cylinder part (excavation unit) from

Table 5.5 Parameters of propulsion unit and soil condition

D [m]	Diameter	0.13
H_L [m]	Length of the excavation unit	0.443
K	Coefficient of earth pressure	0.7
W [N]	Weight	0 − 80
γ_Z	Density	10.78×10^3
μ	Coefficient of friction between soil and excavator	0.65

deep excavation.

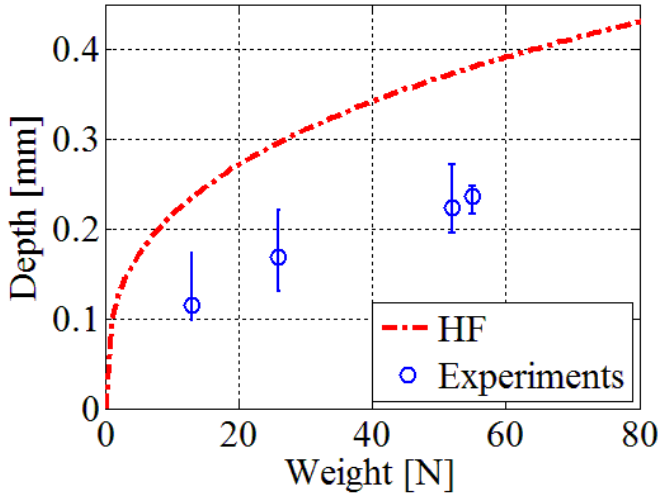

Fig. 5.23 Comparisons of model and experiments

5.6.4 Conclusion of Experiments with Excavation Unit

Throughout these first experiments, the excavation unit as tested alone (i.e., without the propulsion unit as added in a later phase—see the following) was able to excavate to quite a depth with a large weight. The unit can excavate to a similar depth, but faster, when the EA rotates faster. It was confirmed that the friction caused by soil, piled up around the body of the unit, decreases the pushing force of this type of excavator, and limits its ability to excavate deeper. The reachable excavation depth totally depends upon the pushing force. This was also demonstrated from the model of depth prediction by the earth pressure. Thus one strategy to enable the unit to dig deeper is to increase the mass of the excavator. It is not possible, however, to rely on mass alone under gravity conditions such as those on the Moon. Thus an additional mechanism is required to decrease the effect of the friction generated from the piled up soil. Therefore, it is required to develop a propulsion unit that also maintains the orientation of the body position against a maximum rotation reaction force of around 18 Nm. This value would be decreased with a propulsion unit because the movement of a subunit can be controlled.

The power P W is calculated at the maximum rotation reaction force of 18 Nm. It is given as follows:

$$P = 2\pi nT \tag{5.45}$$

Here, n (r/sec) is the rotation speed of the EA per second, T (Nm) is the torque. Therefore the power was 18.8 W.

Chapter 6: Development of a Propulsion Unit

6.1 Development of a Propulsion Subunit

A variety of earthworm robots have been developed using different actuators such as an air pressure type of EWM [80] (Fig. 6.1), SMA type of artificial earthworm prototype [81] (Fig. 6.2), the micro-robot of magnetic field type [82] (Fig. 6.3), the air-emit robot using artificial muscles and air pressure [83] (Fig. 6.4), the worm-like robot with discrete actuators surrounded by a braided mesh [84] (Fig. 6.5), with some motors being suitable for an explorer operating in a vacuum and for use in

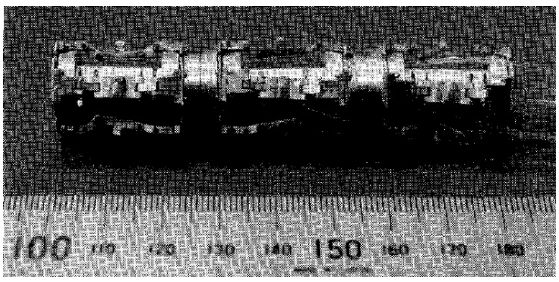

Fig. 6.1 EWM [80]

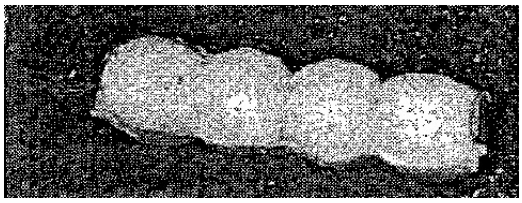

Fig. 6.2 Artificial earthworm prototype (SMA) [81]

Fig. 6.3 Micro-robot [82]

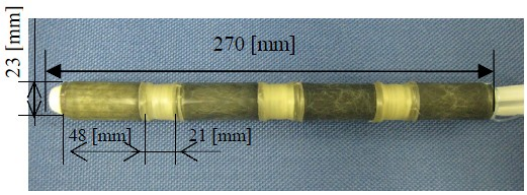

Fig. 6.4 Air-emit robot [83]

Fig. 6.5 Worm-like robot with discrete actuators surrounded by a braided mesh [84]

conditions where temperatures vary widely. Taking these developments into account, an earthworm robot that was developed uses servomotors and can move downwards as well as upwards in perforated soil [85]. Initially, this robot was neither equipped with an excavation tool for boring holes in the soil, nor could generate enough force to withstand the rotation action of the excavation unit.

A new propulsion unit was required to resist the maximum rotation action of the excavation unit and supply the appropriate weight to balance the vertical force of the robot mass, and therefore, a propulsion element (a subunit or an actuated ring) was developed corresponding to a single segment of a natural earthworm. Fig. 6.6 shows the structure of this device. The subunit has two stepper motors and ball screws (MB0401, KSS) to: 1) generate contraction and extension forces that are large enough to withstand the rotary action of the excavation unit; and 2) move plate A with respect to parallel plate B to enable smooth contraction and extension movements. The stepper motors and ball screws control the contraction and extension of the actuated ring. As the subunit contracts, a dual pantograph extends in the radial direction. An expansion plate is attached to the dual pantograph, and this expansion plate also expands in the radial direction, thus it can push in parallel against the surface of the walls of a hole (Fig. 6.7). In addition, the expansion plate has a large circular arc area to maintain contact with the wall surface, which maintains body position during the rotation action of the EA ((c) in Fig. 6.7). The subunit has two actuators and a large space of 65 mm in diameter, thus allowing for an additional transport mechanism to be located in the centre of the unit. Fig. 6.8 showed a developed subunit along the design and Table 6.1 lists its specifications.

The expansion force of the dual pantograph shown in Fig. 6.9 is given in (6.1), where the expansion force is F, the contraction force is W and the arm angle is θ. From this equation, it can be seen that when the unit fully contracts, the expansion force is maximum.

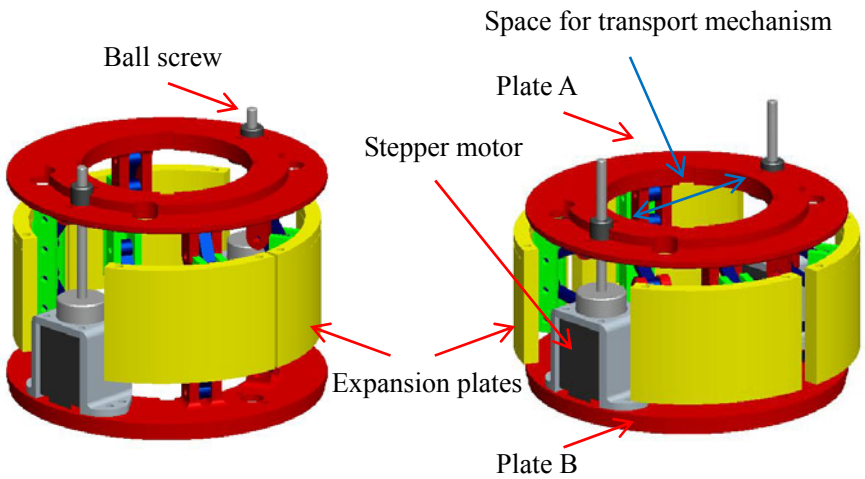

a) Extension b) Contraction

Fig. 6.6 Developed subunit, a ring actuated by dual pantographs

$$F = \frac{W}{\tan\theta} \tag{6.1}$$

Fig. 6.10 shows the controlling system of a subunit which has two stepper motors. A motor driver controls the velocity and rotation direction of the motors. The main controller for the driver is the H8/3052F using the PWM. C program is used to control the system.

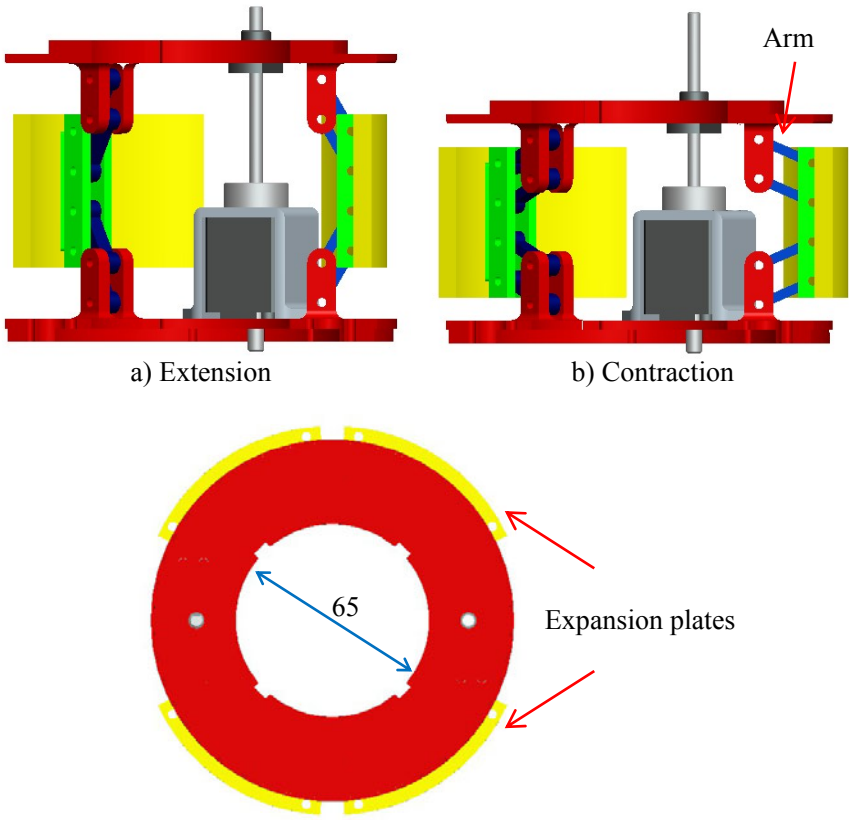

a) Extension b) Contraction

c) Top view

Fig. 6.7 Mechanism of dual pantograph

Table 6.1 Specifications of a unit

Max plate distance [mm]	84.0
Minimum plate distance [mm]	46.5
Max thickness [mm]	144
Minimum thickness [mm]	124
Diameter of space [mm]	65.0
Mass [kg]	0.51
Material	ABS

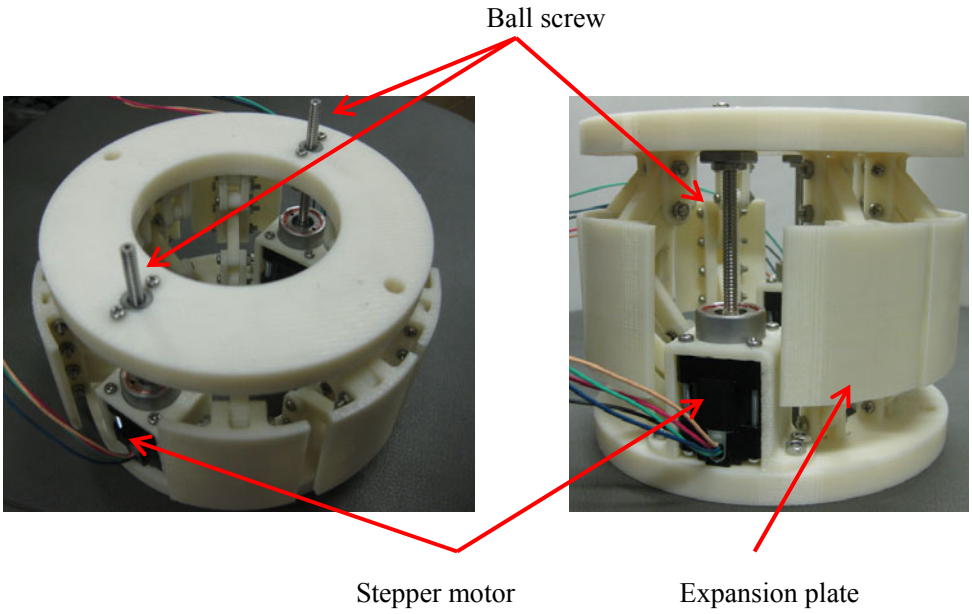

Fig. 6.8 Unit and mechanism of dual pantograph

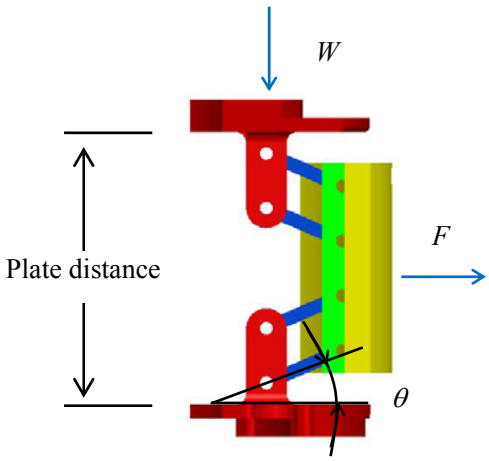

Fig. 6.9 Expansion force of a unit

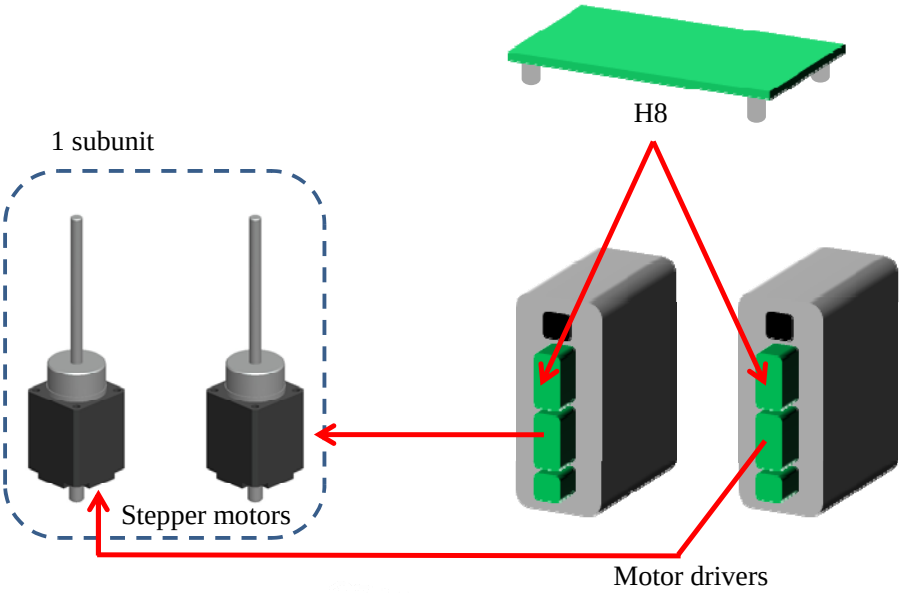

Fig. 6.10 Controlling system of a subunit

6.2 Experiments with Actuated Ring

A prototype excavation robot that was developed, moves inside a launcher (a tube providing initial support and guidance) and digs a hole in a tube initially full of soil. In this subsection, experiments were carried out to test whether an actuated ring can resist the rotary action of the excavation unit and ensure the vertical reaction force necessary to balance the weight of the robot.

First, measuring values were the extension and contraction forces of the unit and the expansion force that the unit exerts on the walls of the hole using a load cell (LUB-500KB, KYOWA) as illustrated by (a) in Fig 6.11. The extension force and contraction force in the radial direction corresponded to W in Fig. 6.9 and were measured as 55 N, almost the same, regardless of the plate distance. Thus, the expansion force was obtained as illustrated by (b) in Fig 6.11. Fig. 6.12 shows the experimental results of the expansion force and the calculated values. These calculated values are obtained from (6.1) with W taken as 55 N, as measured previously. Thus, in practice, the actuated ring generates nearly the same thrust force as the calculated values.

Next, the rotation action and the vertical support force of the unit were measured. Experiments were conducted inside a launcher 131 mm in diameter and in a dirt hole 130 mm in diameter. Fig. 6.13 shows the experimental conditions. The reaction force resulting from the ring balances the rotation action of the EA. The vertical support force supports the weight and the propulsion force caused by the EA during excavation. In measuring the vertical support force, a unit was positioned in the contracted state inside the launcher and dirt hole, and the contracted unit's expansion plates are in